SATIF-15:
15th Workshop on Shielding aspects of Accelerators, Targets, and Irradiation Facilities

Facility for Rare Isotope Beams (FRIB) at Michigan State University
East Lansing, Michigan USA
20-23 September 2022.

Poster Session

Table of contents

1. Modelling of Multilayer Shielding Scenario for High Energy Neutron Accelerator-Based using PHITS

Fitrotun Aliyah[1,2]*, Azhar Abdul Rahman[1]*, Yasmin Md Radzi[1], Imam Kambali[3]
[1]School of Physics, Universiti Sains Malaysia, Penang, Malaysia
[2]Department of Nuclear Engineering and Engineering Physics, Universitas Gadjah Mada, Yogyakarta, Indonesia
[3]Research Center for Accelerator Technology, National Research and Innovation Agency, Indonesia
*Corresponding author: fitrotun.aliyah@student.usm.my/fitrotun.aliyah@ugm.ac.id, arazhar@usm.my

Neutron shielding calculations have complex challenges that require conservative planning in designing shielding to meet radiation protection standards. So far, hydrogenous materials such as concrete, water, and polyethylene have been chosen against neutron radiation. However, these materials will require a thick shielding design that increases the footprint and cost requirements in high-energy neutron sources. Therefore, this paper will model a multi-layer shielding scenario for high-energy neutron sources using metal and hydrogenous materials such as Fe, Cu, concrete, and borated polyethylene. Parameter data from simulation results are the distribution of neutron flux, spectrum energy, neutron depth dose, and ambient dose H(10) equivalent. The simulation results show that Cu is most effective in attenuating high-energy neutrons despite having the highest build-up factor value. Meanwhile, the multilayer combination of Fe-Fe-BPE and Fe-concrete-BPE provides the best choice compared to other material combination scenarios with the lowest flux values and ambient dose H*(10) equivalent rate.*

1.1. Introduction

Neutron is one of the ionizing radiations with a tremendous radiation hazard impact on human health (Mansouri *et al.*, 2020). Neutrons have a greater Linear Energy Transfer (LET) value than alpha, beta, gamma, and X-ray radiation, which causes irreversible damage at the organ DNA level (Kaçal, Akman and Sayyed, 2019; Aliyah, Pinasti and Rahman, 2021). Therefore, shielding is crucial to protect humans and the environment from the dangers of this radiation. Neutrons are produced not only from nuclear reactors but from the accelerator for the radioisotope production industry and health facilities that utilize high-energy nuclear radiation in diagnostics, radiotherapy, and nuclear medicine.

The neutron radiation shielding design calculation is more complex than gamma ray or X-ray. The type of interaction between the neutron and the matter also the neutron energy causes the challenge. Based on their energy, neutrons are classified into several levels. A neutron with more than 1 MeV energy is called a fast neutron (Mansouri *et al.*, 2020; Piotrowski, 2021). Due to no charge, neutrons can pass through the material by interacting or escaping. Neutrons interact with the nucleus of matter through three mechanisms: inelastic scattering, elastic scattering, and absorption or capture (Hu, Hu, *et al.*, 2020; Hu, Shi, *et al.*, 2020). For fast neutrons, it is impossible to stop the neutrons by absorption. Therefore, a neutron attenuation mechanism is needed to reduce the neutron energy from fast neutrons to thermal neutrons, which can then be captured (absorption). Attenuation of fast neutrons generally occurs through scattering reactions (inelastic and elastic) (Piotrowski, 2021).

Inelastic scattering occurs when neutrons collide with atomic nuclei and form a cluster of nuclei, followed by the emission of gamma rays and lower-energy neutrons. As a result of the inelastic scattering reaction, the neutron energy decreases from fast to intermediate neutrons. When it reaches the intermediate threshold, the neutrons will be slowed down

until they become thermal neutrons through elastic scattering. Inelastic scattering is typical in heavy nuclei because they have many energy levels allowing this interaction. In comparison, elastic scattering dominates the interaction of neutrons with low atomic nuclei, such as hydrogen or hydrogenous material (concrete). In elastic scattering, only occurs kinetic energy transfer. After the neutrons reach the thermal level, the neutrons will be absorbed by the shielding material. The probability of neutron capture does not depend on the material density but on its macroscopic cross-section value. Based on the explanation of the neutron interaction mechanism above, the choice of shielding material needs to be considered to maximize shielding effectiveness based on the type of material and interaction. Traditional shielding employs a single type of material, but composite and multilayer shielding uses various materials and components to create a radiation-resistant barrier better than conventional shielding. This allows the shielding thickness to be significantly reduced.

The concept of combining several shielding materials is generally carried out in two ways: making a new material in a composite form consisting of a mixture of various types of materials or combining a single layer of material in a multilayer structure (Arif Sazali, Alang Md Rashid and Hamzah, 2019). However, the challenge in making composites is that it is difficult to create homogeneity in the mixture, so there is concern that there are pinholes that allow radiation to pass through the gaps (Kim, Park and Seo, 2015). In addition, the manufacture of new composite materials also has challenges in the inconsistency of radiation shielding performance (Osman *et al.*, 2015; Wang *et al.*, 2015). The multilayer shielding approach is often preferred to overcome this problem (Park *et al.*, 2018; Daneshvar *et al.*, 2021; Ma *et al.*, 2021).

The multilayer shielding concept has been used since 1943, namely in the moderator material of the Chicago reactor, which used concrete and paraffinized wood. The shielding can counteract the mixed radiation from neutrons and prompt gamma-ray (Arif Sazali, Alang Md Rashid and Hamzah, 2019). After that, the use of multilayer shielding continued to increase, where its application was not only limited to nuclear radiation shielding but also used for open-scape satellites (Daneshvar *et al.*, 2021; Gohel and Makwana, 2022) and electromagnetic shielding (Hu *et al.*, 2022; Li and Sun, 2022; Li *et al.*, 2022; Mikinka and Siwak, 2022). In 2010, MS Hossain et al. used poly boron (PB) and borax mixed concrete (BX) as neutron shielding from a ^{252}Cf source. The results of his study show that multilayer shielding PB+BX performed better than a single layer (S. Hossain *et al.*, 2010). A decade later, Guang Hu et al. (2020) conducted a multilayer shielding design study with a combination of PE, B_4C, and Pb materials for secondary radiation neutrons and gamma rays from proton sources using Monte Carlo MCNP simulations and genetic algorithms (GA) (Hu, Hu, *et al.*, 2020). Yin Shang et al. (2020) used multilayer structure from high-density polyethylene/hexagonal boron nitride (HDPE/hBN) layers and low-density polyethylene (LDPE) layer as a high neutron shielding material. The result shows that the multi-layered PE/hBN films have excellent neutron shielding performance through multiple repeated scattering, absorption, and dissipation between multilayers (Shang *et al.*, 2020). Meanwhile, Baolong Ma et al. (2021) developed a multilayer design with lead (Pb) and borated polyethylene (BPE) materials for compact accelerator-driven neutron sources (CANS), which indicated that the proposed design could reduce the shielding weight by up to 60% (Ma *et al.*, 2021).

A comprehensive review related to multilayer shielding has been carried out (Arif Sazali, Alang Md Rashid and Hamzah, 2019). Various material combinations have been used as multilayer shielding for several radiation sources and energy ranges. For instance, lead, polyethylene, boron carbide, and iron for a fission spectrum of ^{235}U (Cai *et al.*, 2018); composites from a polymer containing tungsten or bismuth-tin alloy with BiSn layered sheet for X-ray shielding (Park *et al.*, 2018); Concrete and Iron contained aggregate

materials (FeB, Fe_2B, stainless steel) for proton sources (Sariyer and Küçer, 2018); lead and HDPE for ^{252}Cf sources (Hadad *et al.*, 2016); Polyethylene and steel for the neutron energy range of 1~14 MeV (Whetstone and Kearfott, 2016); Epoxy ilmenite and Boron oxide glass for ^{252}Cf sources (Gaber, El-Sarraf and Kansouh, 2013); and many other multilayer combinations. As far as the literature study has been conducted, there has been no investigation of multilayer shielding for high energy neutrons of around 200 MeV or more. Currently, more facilities use high-energy neutrons in industry and health facilities, such as proton therapy, carbon ion, and hadron therapy. This study aims to determine the effectiveness of multilayer shielding with various structural combinations of Fe, Cu, concrete, and borated polyethylene (BPE) materials at a high-energy neutron source of around 200 MeV. The distribution of flux, effective dose, and ambient dose equivalent of each shielding scenario will be discussed in this study.

1.2. Materials and Methods

This research was conducted through a Monte Carlo simulation using the Particle Heavy Ion Transport Code System (PHITS). The 2D geometry design is shown in Figure 1.1, and the programming flow is illustrated in Figure 1.2. A neutron source with an energy of 200 MeV, 1 µA beam current, was placed 50 cm from the shielding material. The neutron source was assumed as a pencil beam. Paraffin was used as a neutron beam collimator material, and the air or void was the medium between the source and barriers. In this simulation, the shielding was represented by a cylindrical slab with 30 cm thickness, forming a total thickness of 90 cm. The number of particles in this simulation was 10^6, with maxcas 10^5 and maxbch 10^1. The history numbers were employed to eliminate uncertainty errors kept below 2%.

The materials used were Fe (7.7 g/cm^3), Cu (8.96 g/cm^3), concrete (2.2 g/cm^3), and Borated Polyethylene (0.94 g/cm^3). The details of the atomic ratio and density of materials are listed in Table 1.1. The PHITS code models neutron transport through shielding materials with various interactions using cross-section data from the JENDL-4.0 libraries. First, the simulation begins by creating an input file. In this study, the input file consists of several sections named parameters, source, material, mat name color, surface, cell, t-tract, t-cross, and importance. Determination of parameters in the input file includes calculation mode, number of particle numbers, number of batches, PHITS install folder name, and general output file name. Then, on the source card, we determined the source type number based on the geometry, projectile, beam energy, beam direction, and the neutron source's coordinate position. The s-type was 1, meaning the neutron was a mono-energetic axial source. The direction of the projectile was dir=1, indicating the direction cosine of the projectile against the z-axis. Then the material section was used to define the material number, nuclides, composition ratios, and color in Mat name color for exciting visualization. While the material densities were provided in the cell section. The setting of geometry was done in the cell and surface sections. The T-tract tally was used to display the neutron flux distribution through the shielding material, the profile of the effective dose, and the ambient dose equivalent. The unit for ambient dose was Sv/h with a normalization factor of 2.25e4. The H*(10) multiplier ID and effective dose based on ICRP103 (AP irradiation) were -200 and -202, respectively. At the same time, the t-cross was performed to display the energy spectrum of neutrons and flux when passing through the shielding material. The importance was applied to determine the particle's weight for variance reduction. The execution uses the INCL model (Boudard *et al.*, 2013), the EGS5 code (Hirayama *et al.*, 2005), and the KUROTAMA model (Iida, Kohama and Oyamatsu, 2007) found in PHITS version 3.02 and above (Sato *et al.*, 2018).

Figure 1.1. 2D geometry layout

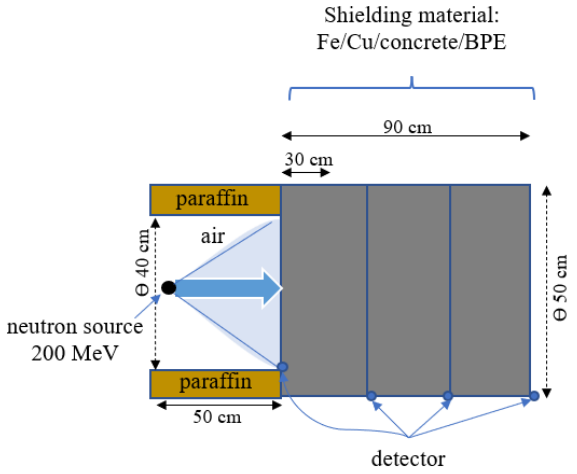

Figure 1.2 Simulation process using PHITS

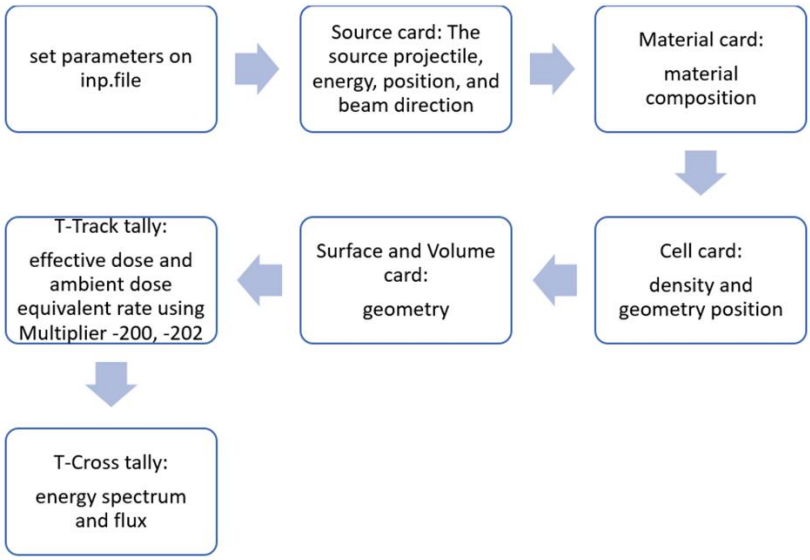

This study carried out a two-stage simulation; the first was performed using one type of material, and the second used a combination of several types of materials with a multilayer concept. There were twelve scenarios of multilayer structure combinations that were modelled. The distribution of neutron flux and ambient dose equivalent H*(10) will be evaluated from all scenarios. The best scenario was the lowest H*(10) value. Furthermore, the H*(10) value based on radiation protection regulation will be used to determine the thickness of the shielding material using Portland concrete to compare the effectiveness of multilayer shielding with traditional concrete shielding.

In the multilayer structure shield shown in Figure 1.3, the radiation intensities evolving from the following layers are reliant on the former layers. The I_3 as the resultant intensity can be obtained from the following Equation (Al-Arif and Kakil, 2015).

$$I_3 = I_0 e^{-\Sigma(\Sigma_t x)}$$

$$I_3 = I_0 B e^{-\Sigma(\Sigma_t x)}$$

$$I_3 = I_0 B_1 B_2 B_3 e^{-(\Sigma t_1 x_1 + \Sigma t_2 x_2 + \Sigma t_3 x_3)}$$

Figure 1.3. A simple schematic of multilayer shielding (modified from Al-Arif and Kakil, 2015)

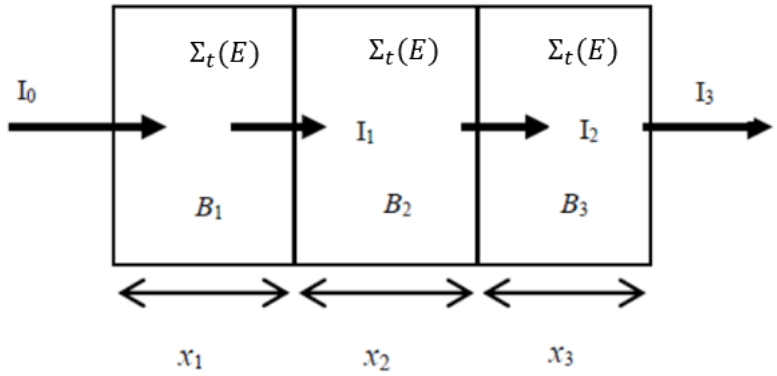

I_0 is the radiation intensity without shielding, Σ_t is the neutron total macroscopic cross-section, x is the shielding thickness, and B is the build-up factor. Several researchers have empirically estimated the build-up factor value, which depends on the Z value of the atoms in each layer (Burke and Beck, 1974; Shin and Hirayama, 1995; Mann, Heer and Rani, 2016).

Table 1.1. materials properties of this study

Material	Density *g/cm^3)	Atomic fraction
Cu	8.96	1.0
Fe	7.7	1.0
Concrete (Garcia-Fernandez *et al.*, 2021)	2.2	^{1}H (0.023), ^{12}C (0.019), ^{16}O (0.530), ^{27}Al (0.034), ^{28}Si (0.337), ^{40}Ca (0.044), ^{56}Fe (0.014)
BPE (Ma *et al.*, 2018)	0.94	^{1}H (0.644), ^{12}C (0.322), ^{16}O (0.022), ^{10}B (0.003), ^{11}B (0.011)

1.3. Result and Discussion

The simulation of multilayer shielding design for 200 MeV high energy neutron sources has been carried out using the PHITS code. Figure 1.4 shows the effective dose in single layer shielding across the thickness of the material. The graph shows that the effective dose comes from dominantly neutron radiation and gamma-ray emission, a marginal dose. Cu has the smallest effective dose compared to other materials at the same thickness, followed by Fe, concrete, and BPE. However, the build-up factor in Cu material is enormous, affecting the resultant radiation intensity behind the multilayer shielding later. Those are consistent with the theory that the denser material (high Z atomic value), the higher the chance of inelastic scattering, so the greater the gamma rays produced from scattering. While Fe shows a lower build-up region than Cu at 90 cm depth, it has almost the same gamma dose rate. Concrete and BPE have similar effective dose profiles due to hydrogenous material.

Figure 1.4. Effective dose in shielding depth for neutron and photon radiation

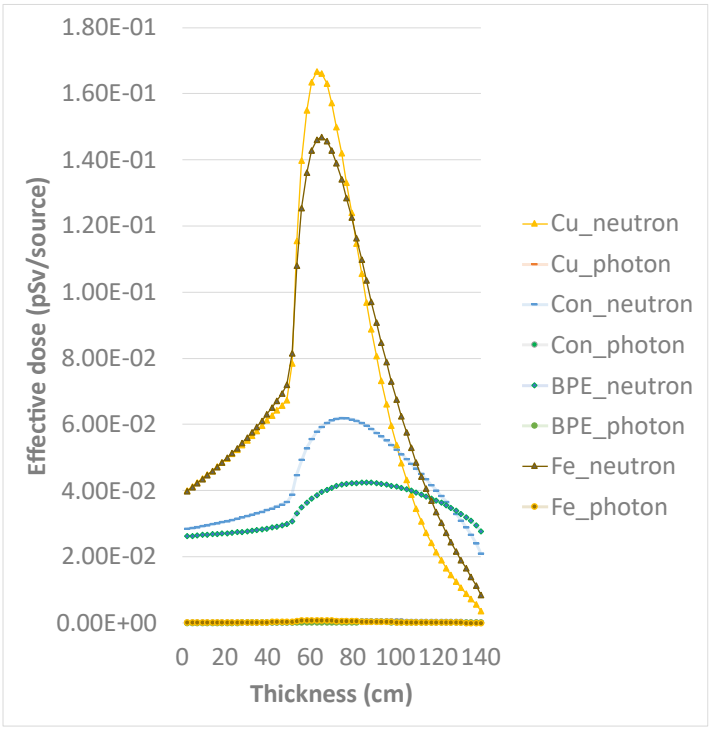

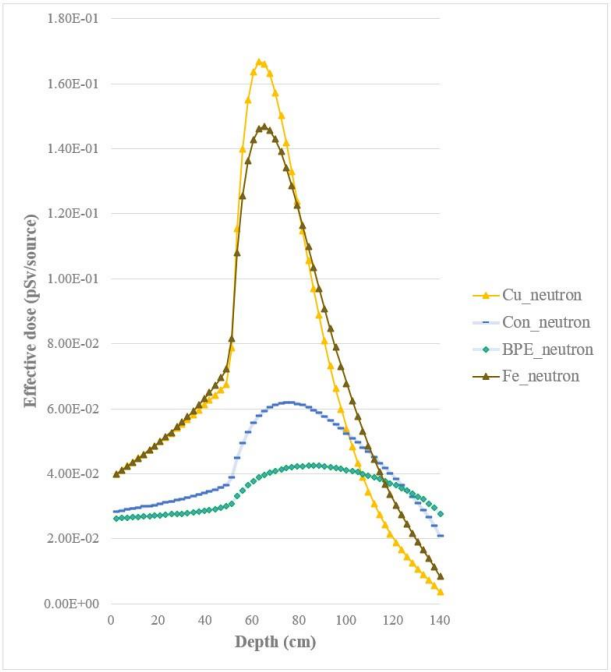

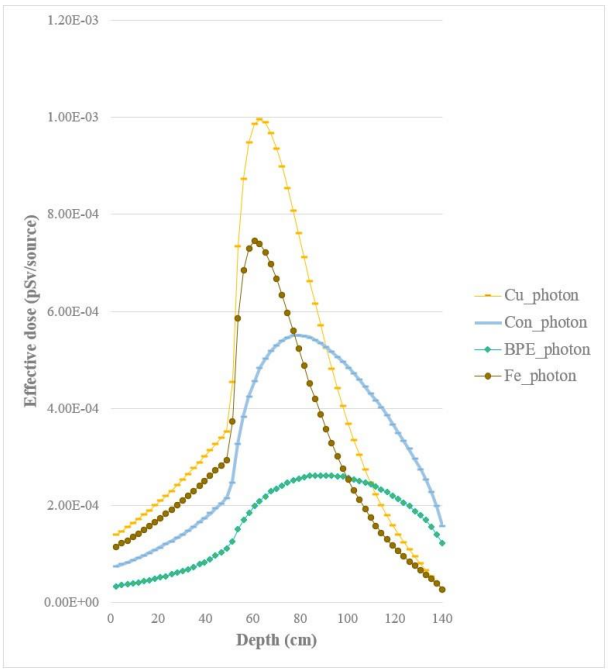

Meanwhile, Figure 1.5 shows neutron flux distribution in various multilayer structure scenarios. Different layer arrangements give diverse neutron flux profiles. As a result of the sequential placement of multilayer slabs, the attenuation of each slab influences the multilayer curve. Changing the type of slab abruptly alters the attenuation. This is how the created curves lost their smoothness (S. Hossain *et al.*, 2010). Low Z first and high Z first has different effect. The peak value means that more neutrons are available. When low Z material was placed in the first layer (concrete in the first layer), the neutron flux in the shallow depth was lower than the reverse shield. However, at the end of multilayer depth,

neutron flux significantly increases and is higher than the reverse structure. Conversely, when Fe and Cu were placed in the initial layer, the neutron flux was higher in the first layer and dropped dramatically. An exciting thing comes from the Fe-BPE-concrete arrangement. In the BPE layer, the presence of neutrons significantly shortens due to capturing by the BPE material, where boron has a high absorption cross-section.

Figure 1.5. Neutron flux distribution in depth

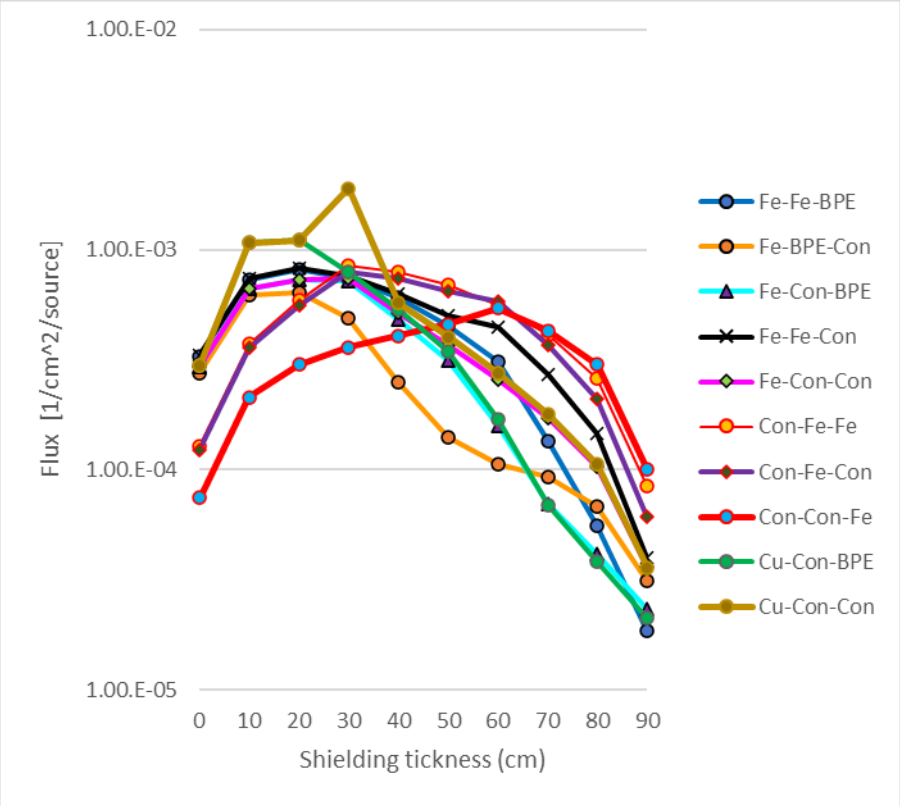

Table 1.2 presents the ambient dose equivalent rate values from various multilayer scenarios. These results found that the difference in arrangement causes a significant difference in the shielding performance. For high-energy neutrons, placing hydrogenous material in the first layer produces a higher ambient dose than the opposite order. Fe in the first arrangement, followed by hydrogenous material, was better than in other scenarios. The leading group with the lowest ambient dose equivalent rate was the multilayer structure of Fe as the first arrangement, except for the Fe-BPE-concrete arrangement.

Interestingly, although Cu has maximum performance as shielding high energy neutrons when combined with hydrogenous material concrete and BPE, it has worse performance than the combination of Fe+hydrogenous. Double Cu layer +concrete has a slightly different ambient dose rate than Fe+double concrete, which has the value of 9.25E+01 Sv/h and 9.30E+01 Sv/h, respectively. From economic considerations, the choice of Fe+concrete+concrete is outstanding because it is more affordable than Cu+Cu+concrete. Therefore, the scenario of Fe in the first layer will be used in the simulation's second stage, which will be compared with the traditional shielding concrete layer.

Table 1.2. Ambient dose equivalent, H*(10)

Multilayer shielding scenario	H*(10), Sv/h
Fe-Fe-BPE	4.98E+01
Fe-BPE-Concrete	1.07E+02
Fe-Concrete-BPE	8.19E+01
Fe-Fe-Concrete	6.02E+01
Fe-Concrete-Concrete	9.30E+01
Concrete-Fe-Fe	2.48E+02
Concrete-Fe-Concrete	1.23E+02
Concrete-Fe-BPE	2.44E+02
Concrete-Concrete-Fe	3.58E+02
Cu-Concrete-BPE	1.62E+02
Cu-Concrete-Concrete	1.86E+02
Cu-Cu-Concrete	9.25E+01

The subsequent calculation was performed by varying the thickness of each Fe+concrete+BPE layer arrangement and the single-layer conventional shielding concrete. The ambient dose rate values for the two designs were 0.4329 Sv/h and 0.4319 Sv/h for Fe-Concrete-BPE (100-150-30 cm) and 455 cm of concrete, respectively. It was found that the decrease in multilayer shielding structures was around ~38.5% compared to traditional single-layer shielding concrete. This figure is beneficial for reducing land requirements and footprint in building facilities that utilize high-energy neutrons. In addition, reducing shielding thickness lowers the construction material required; hence this multilayer design minimizes CO_2 emissions.

1.4. Summary and Conclusions

A multilayer shielding design for a high-energy neutron accelerator was successfully simulated using PHITS. The layer arrangement placement significantly impacts the effectiveness and performance of radiation shielding. High Z material in the first layer yields a lower neutron flux than its counterpart for high-energy neutron shielding. The ambient dose equivalent rate computation demonstrates that the Fe material in the first layer is superior to Cu or concrete. Cu delivers the lowest effective dose for high-energy neutron shielding, although it does not function well in multilayer shielding. Fe-Fe-BPE, Fe-Fe-Concrete, and Fe-Concrete-BPE exhibit lower flux and ambient dose values than other material combination structures. Multilayer Fe-concrete-BPE (100-150-30) cm is comparable to 455 cm of conventional concrete shielding, or 38.5% less than typical shielding thickness.

1.5. Acknowledgment

The authors are grateful for the Malaysian Ministry of Higher Education's financial support through the Malaysia International Scholarship program.

1.6. List of references

Al-Arif, M. and Kakil, D. (2015) 'Calculated-Experimental Model for Multilayer Shield', *Aro, The Scientific Journal of Koya University*, 3(1), pp. 23–27. doi: 10.14500/aro.10057.

Aliyah, F., Pinasti, S. G. and Rahman, A. A. (2021) 'Proton therapy facilities: an overview of the development in recent years', *IOP Conference Series: Earth and Environmental Science*, 927(1), p.

012042. doi: 10.1088/1755-1315/927/1/012042.

Arif Sazali, M., Alang Md Rashid, N. K. and Hamzah, K. (2019) 'A review on multilayer radiation shielding', *IOP Conference Series: Materials Science and Engineering*, 555(1). doi: 10.1088/1757-899X/555/1/012008.

Boudard, A. *et al.* (2013) 'New potentialities of the Li\`ege intranuclear cascade model for reactions induced by nucleons and light charged particles', *Physical Review C*, 87(1), p. 14606. doi: 10.1103/PhysRevC.87.014606.

Burke, G. de P. and Beck, H. L. (1974) 'Calculated and Measured Dose Buildup Factors for Gamma Rays Penetrating Multilayered Slabs', *Nuclear Science and Engineering*, 53(1), pp. 109–112. doi: 10.13182/NSE74-A23334.

Cai, Y. *et al.* (2018) 'A method to optimize the shield compact and lightweight combining the structure with components together by genetic algorithm and MCNP code', *Applied Radiation and Isotopes*, 139(December 2017), pp. 169–174. doi: 10.1016/j.apradiso.2018.05.009.

Daneshvar, H. *et al.* (2021) 'Multilayer radiation shield for satellite electronic components protection', *Scientific Reports*, 11(1), pp. 1–12. doi: 10.1038/s41598-021-99739-2.

Gaber, F. A., El-Sarraf, M. A. and Kansouh, W. A. (2013) 'Utilization of boron oxide glass and epoxy/ilmenite assembly as two layer shield', *Annals of Nuclear Energy*, 57, pp. 106–110. doi: 10.1016/j.anucene.2013.01.036.

Garcia-Fernandez, G. F. *et al.* (2021) 'Neutron dosimetry and shielding verification in commissioning of Compact Proton Therapy Centers (CPTC) using MCNP6.2 Monte Carlo code', *Applied Radiation and Isotopes*, 169(July 2020), p. 109279. doi: 10.1016/j.apradiso.2020.109279.

Gohel, A. and Makwana, R. (2022) 'Multi-layered shielding materials for high energy space radiation', *Radiation Physics and Chemistry*, 197(December 2021), p. 110131. doi: 10.1016/j.radphyschem.2022.110131.

Hadad, K. *et al.* (2016) 'Moderation and shielding optimization for a 252Cf based prompt gamma neutron activation analyzer system', *International Journal of Hydrogen Energy*, 41(17), pp. 7221–7226. doi: 10.1016/j.ijhydene.2015.12.208.

Hirayama, H. *et al.* (2005) *The EGS5 Code System*, *Kek*.

Hu, G., Shi, G., *et al.* (2020) 'Development of gradient composite shielding material for shielding neutrons and gamma rays', *Nuclear Engineering and Technology*, 52(10), pp. 2387–2393. doi: 10.1016/j.net.2020.03.029.

Hu, G., Hu, H., *et al.* (2020) 'Study on the design and experimental verification of multilayer radiation shield against mixed neutrons and γ-rays', *Nuclear Engineering and Technology*, 52(1), pp. 178–184. doi: 10.1016/j.net.2019.07.016.

Hu, G. *et al.* (2022) 'Ultrathin nanocomposite films with asymmetric gradient alternating multilayer structures exhibit superhigh electromagnetic interference shielding performances and robust mechanical properties', *Chemical Engineering Journal*, 447(March), p. 137537. doi: 10.1016/j.cej.2022.137537.

Iida, K., Kohama, A. and Oyamatsu, K. (2007) 'Formula for Proton–Nucleus Reaction Cross Section at Intermediate Energies and Its Application', *Journal of the Physical Society of Japan*, 76(4), p. 44201. doi: 10.1143/JPSJ.76.044201.

Kaçal, M. R., Akman, F. and Sayyed, M. I. (2019) 'Evaluation of gamma-ray and neutron attenuation properties of some polymers', *Nuclear Engineering and Technology*, 51(3), pp. 818–824. doi: 10.1016/j.net.2018.11.011.

Kim, Y., Park, S. and Seo, Y. (2015) 'Enhanced X-ray Shielding Ability of Polymer–Nonleaded Metal

Composites by Multilayer Structuring', *Industrial & Engineering Chemistry Research*, 54(22), pp. 5968–5973. doi: 10.1021/acs.iecr.5b00425.

Li, M. *et al.* (2022) 'Multilayer structured CNF/rGO aerogels and rGO film composites for efficient electromagnetic interference shielding', *Carbohydrate Polymers*, 286(December 2021), p. 119306. doi: 10.1016/j.carbpol.2022.119306.

Li, Y. T. and Sun, Y. T. A. (2022) 'An investigation of electromagnetic interference shielding effectiveness with multilayer thin films material', *Thin Solid Films*, 753(October 2021), p. 139259. doi: 10.1016/j.tsf.2022.139259.

Ma, B. *et al.* (2018) 'Shielding design of a target station and radiation dose level investigation of proton linac for a compact accelerator-driven neutron source applied at industrial sites', *Applied Radiation and Isotopes*, 137(28), pp. 129–138. doi: 10.1016/j.apradiso.2018.03.015.

Ma, B. *et al.* (2021) 'Multiobjective Optimization Shielding Design for Compact Accelerator-Driven Neutron Sources by Application of NSGA-II and MCNP', *IEEE Transactions on Nuclear Science*, 68(2), pp. 110–117. doi: 10.1109/TNS.2020.3040500.

Mann, K. S., Heer, M. S. and Rani, A. (2016) 'Gamma-ray double-layered transmission exposure buildup factors of some engineering materials, a comparative study', *Radiation Physics and Chemistry*, 125, pp. 27–40. doi: 10.1016/j.radphyschem.2016.03.001.

Mansouri, E. *et al.* (2020) 'A review on neutron shielding performance of nanocomposite materials', *International Journal of Radiation Research*, 18(4), pp. 611–622. doi: 10.18869/acadpub.ijrr.18.4.611.

Mikinka, E. and Siwak, M. (2022) 'Experimental characterisation and prediction of shielding effectiveness for multilayer carbon fibre reinforced composite materials with varying configurations', *Materials Today Communications*, 32(July), p. 104039. doi: 10.1016/j.mtcomm.2022.104039.

Osman, A. M. *et al.* (2015) 'Studying the shielding properties of lead glass composites using neutrons and gamma rays', *Annals of Nuclear Energy*, 78, pp. 146–151. doi: 10.1016/j.anucene.2014.11.046.

Park, S. *et al.* (2018) 'Multilayer-Structured Non-leaded Metal/Polymer Composites for Enhanced X-ray Shielding', *MRS Advances*. 2018/04/17, 3(31), pp. 1789–1797. doi: DOI: 10.1557/adv.2018.336.

Piotrowski, T. (2021) 'Neutron shielding evaluation of concretes and mortars: A review', *Construction and Building Materials*, 277, p. 122238. doi: 10.1016/j.conbuildmat.2020.122238.

S. Hossain, M. *et al.* (2010) 'Study of shielding behaviour of some multilayer shields containing PB and BX', *Indian Journal of Pure and Applied Physics*, 48(December), pp. 860–868.

Sariyer, D. and Küçer, R. (2018) 'Double-layer neutron shield design as neutron shielding application', *AIP Conference Proceedings*, 1935(1), p. 180004. doi: 10.1063/1.5026020.

Sato, T. *et al.* (2018) 'Features of Particle and Heavy Ion Transport code System (PHITS) version 3.02', *Journal of Nuclear Science and Technology*, 55(6), pp. 684–690. doi: 10.1080/00223131.2017.1419890.

Shang, Y. *et al.* (2020) 'Multilayer polyethylene/ hexagonal boron nitride composites showing high neutron shielding efficiency and thermal conductivity', *Composites Communications*, 19(March), pp. 147–153. doi: 10.1016/j.coco.2020.03.007.

Shin, K. and Hirayama, H. (1995) 'Approximating Model for Multilayer Gamma-Ray Buildup Factors by Transmission Matrix Method: Application to Point Isotropic Source Geometry', *Nuclear Science and Engineering*, 120(3), pp. 211–222. doi: 10.13182/NSE95-A24120.

Wang, P. *et al.* (2015) 'Design, fabrication, and properties of a continuous carbon-fiber reinforced Sm2O3/polyimide gamma ray/neutron shielding material', *Fusion Engineering and Design*, 101, pp. 218–225. doi: 10.1016/j.fusengdes.2015.09.007.

Whetstone, Z. D. and Kearfott, K. J. (2016) 'Layered shielding design for an active neutron interrogation

system', *Radiation Physics and Chemistry*, 125, pp. 69–74. doi: 10.1016/j.radphyschem.2016.03.018.

1.7. List of abbreviations and acronyms

BPE	Borated Polyethylene
LET	Linear Energy Transfer
DNA	Deoxyribonucleic acid
PB	Polyboron
BX	Borax mixed concrete
PE	Polyethylene
MCNP	Monte Carlo N-Particle
GA	Genetic algorithms
HDPE	High-density polyethylene
hBN	hexagonal boron nitride
LDPE	Low-density polyethylene
CANS	Compact accelerator-driven neutron sources
PHITS	Particle Heavy Ion Transport Code System
JENDL	Japanese Evaluated Nuclear Data Library
ICRP	International Commission on Radiological Protection

2. Photon and neutron dose measurements and Monte Carlo evaluation at the Beam Test Facility of the INFN - Frascati National Laboratories

F. Chiarelli, D. Chiti, M. Chiti, R. Donghia*, A. Esposito, A. Raco

National Laboratories of Frascati of INFN, LNF-INFN, Frascati, Italy

*raffaella.donghia@lnf.infn.it

The Beam-Test Facility (BTF) of the INFN - National Laboratories of Frascati (LNF) is an extraction and transport line of DAΦNE LINAC. It is optimized for electron and positron production in a wide range of intensity, energy (30 MeV – 750 MeV), beam spot dimensions and divergence, using both primary and secondary beam of the DAΦNE LINAC.

Through the years, the BTF has gained an important role in particle detectors test and development with electron/positron beam. A small fraction of the BTF's shifts have been dedicated to radiation damage test using LINAC electron primary beam up to 5×10^{10} e^-/s.

As radiation protection group of the LNF, we evaluated the dose when electrons impinging on a Pb target from: i) photon Bremsstrahlung production; ii) photoneutron production. Two dedicated tests with 503 MeV electrons impinging on a ∼16 cm thick Pb target have been carried out in February and June 2022 using TLD700 and TLD600, measuring doses at several charge intervals. The detector response has been calibrated at Cs-137, so that a MC comparison has needed to validate the results at higher energies and benchmark the simulation itself.

The experimental setup, data acquisition and analysis, together with FLUKA modeling of the test are reported below.

2.1. Introduction

The Beam-Test Facility (BTF) of the INFN - National Laboratories of Frascati (LNF) is an extraction and transport line of DAΦNE LINAC. It is optimized for the production of electrons and positrons in a wide range of intensity, energy (30 MeV – 750 MeV), beam spot dimensions and divergence, using both primary and secondary beam of the DAΦNE LINAC.

A mixed field is produced when electrons impinging on a target from: i) photon bremsstrahlung production; ii) photoneutron production. Tests with a ∼ 16 cm thick Pb target have been carried out in February and June 2022 using TLD700 and TLD600, measuring doses at several charge intervals, respectively due to gamma and both gamma and neutron fluence.

The detector response has been calibrated at Cs-137, therefore a MC comparison resulted to be needed to validate the results at higher energies and benchmark the simulation itself.

2.2. The Beam Test Facility of LNF

The Beam Test Facility (BTF) is part of the DAΦNE accelerator complex of the LNF: it is composed of a transfer line driven by a pulsed magnet allowing the diversion of electrons or positrons (usually BTF works in parasitic mode to DAΦNE collider) [1].

The users in BTF are able to know in real time the beam parameters, like particle type, energy, intensity, dimension and position. The facility can produce: electron or positron in single particle and high intensity; "tagged" photons; neutrons.

Our tests have been carried out in the following condition: electrons impinging on a lead target with an energy of 503 MeV, at a rate of 1 Hz and with a charge rate of 1 x 10^9 e^-/s.

2.3. Detector calibration: TLD 700 and 600

Several matrices of TLD700s have been used for the first test (in February 2022) and both TLDs 600 and 700 for the second one (in June 2022) [2]. These detectors show a linear response to a wide photon dose range: from 10 pGy up to 10Gy. The features of these TLDs are summarized in Table 2.1

Table 2.1. Characteristics of the TLD700 and TLD600 from the datasheets

	TLD 700 Lithium Fluoride (^{7}Li isotope) LiF:Mg, Ti	**TLD 600 Lithium Fluoride (^{6}Li isotope) LiF:Mg, Ti**
Radiation type	Beta, Gamma	Beta, Gamma, Neutron
Emission Spectra	3500 to 6000Å (4000 maximum)	3500 to 6000Å (4000 maximum)
Energy Response	1,25 keV/^{60}Co	1,25 keV/^{60}Co
Dimension	0,89 mm x 3,2 mm x 3,2 mm	0,89 mm x 3,2 mm x 3,2 mm
Sensitivity	1.0 at ^{60}Co relative to LiF	1.0 at ^{60}Co relative to LiF
Measurement Ranges	10 pGy to 10 Gy	10 pGy to 10 Gy

The exposure setup is reported in the following sections. After the exposures in BTF, the TLDs have been readout almost instantly using a Risø TL/OSL reader [3]. The readout chosen cycle was: 10 °C/s, up to 300 °C. As example, a typical TLD700 glow curve of counts vs temperature is reported in Figure 2.1. Fading effects have been considered negligible for the test length and “high” dose. We decided to integrate the glow curves in the [110;270] °C region (orange lines in Fig. 1.1), to evaluate the final signal.

For both tests, about 15 TLD700s have been used for calibration at 20 mGy with a 137-Cs source, in order to estimate a counts-to-mGy conversion factor, and 10 TLD700s for background evaluation and subtraction.

In June ‘22, in addition to background and Cs-137 samples, 10 further TLD700s and TLD600s have been exposed to an Am-Be neutron source for calibration purposes. Additional details on this calibration are reported in Section 1.6.

Figure 2.1. ***Example of a TLD700’s glow curve. Vertical lines represent the integration region.***

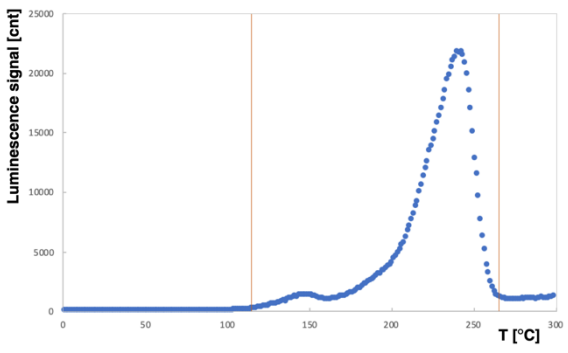

2.4. Experimental setup 1 – February 2022

In addition to the calibration and background dosimeters, 45 TLD700s have been exposed inside the BTF. These were divided in 5 batches (named C, D, E, F, G) and arranged in 3x3 matrices in plastic holders (Fig. 1.2, left). The 5 holders have been placed inside the BTF beyond a ~ 16 cm lead target (Fig. 1.2, right), hit by the 503 MeV electron beam. The BTF laser alignment system has been used for a proper positioning.

The 5 holders have been exposed for different time duration, corresponding to 5 different charge integrals (and kerma), up to a total of 2×10^{12} e^-. The integrated charge per batch is reported in Table 2.2, together with the measurements results in air kerma. The values reported in the third column have been evaluated as the average over the 9 TLDs per batch. In the fourth column, the relating standard deviation is reported. In the last two columns, the same values evaluated from the FLUKA simulations are reported. A more detailed description of the FLUKA model is reported in the following section.

Figure 2.5 shows the air kerma results as a function of the integrated electron charge on the Pb target. A good agreement between data and Monte Carlo is clearly visible.

In this first test configuration, we evaluated a conversion factor of about $(6.1 \pm 0.9) \cdot 10^{-12}$ mGy/e^- from integrated electron charge to mGy, by applying a linear fit on data.

Figure 2.2. Arrangement of the TLDs in the plastic holders (left) and beyond the lead target (right)

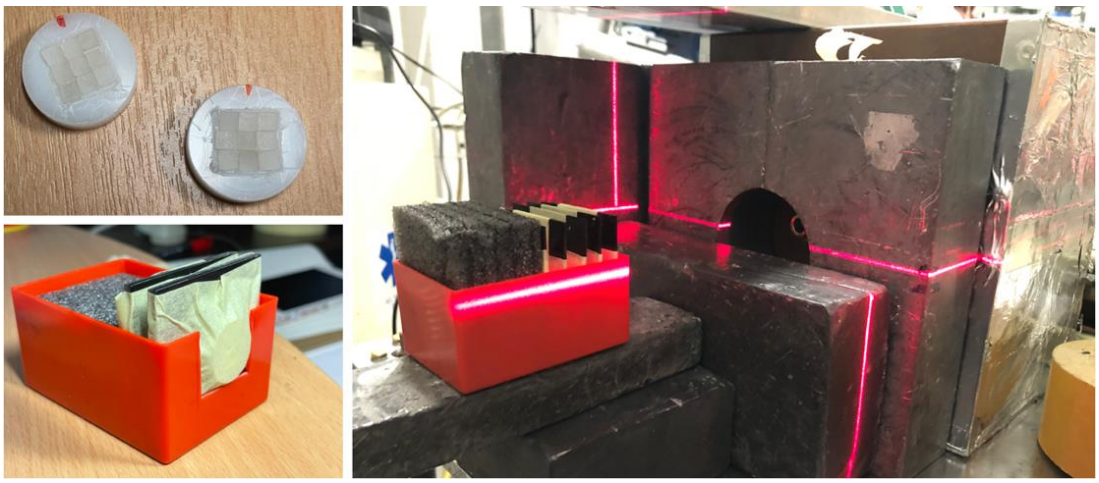

Table 2.2. Summary of the results for each batch of the first test

Batch	Charge [#e^-]	Kerma $_{exp}$ [mGy]	σ_{exp} [mGy]	Kerma $_{FLUKA}$ [mGy]	σ_{FLUKA} [mGy]
C	4.0E+11	3.31	0.83	2.57	0.15
D	8.0E+11	5.60	1.30	5.28	0.25
E	1.2E+12	7.34	2.17	7.82	0.36
F	1.6E+12	9.85	2.64	10.12	0.44
G	2.0E+12	14.53	2.28	12.36	0.54

Figure 2.3. Data-MC comparison of the measured kerma as a function of the integrated primary beam charge impinging on the lead target

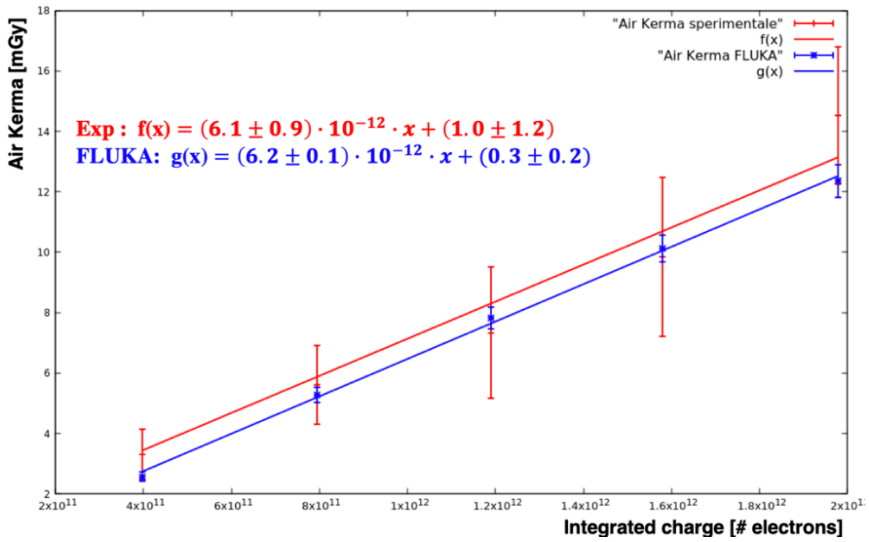

Figure 2.4. Top view (3D model) of the FLUKA experimental setup model on left (right)

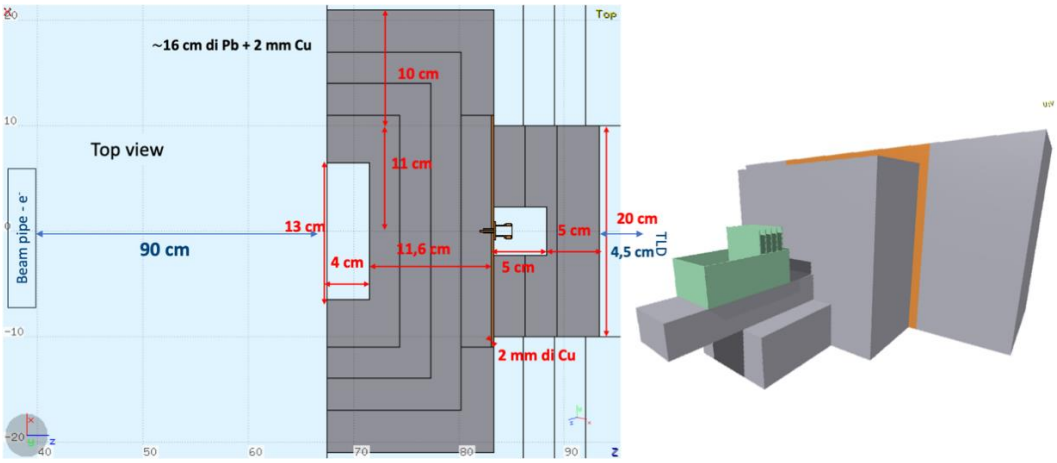

2.5. FLUKA simulation

A complete Monte Carlo model of both the setup has been performed using FLUKA (version 2021.2.5) [4,5]. This describes and includes details on: electron beam (energy and spot size); geometrical layout of the room, target and detectors (within 0.1 mm precision), as shown in Figure 2.4; transport threshold set at 1 keV for $e^{+/-}$ and γ; TLD geometry and material (with the correct enriched Lithium with 99.9% of ^{7}Li); photonuclear cross section libraries.

Figure 2.5 compares the photon (left) and electron (right) spectra per primary electron entering in each TLD of the 5 batches, considering the positioning one behind the other. The attenuation through the different batches is negligible for energy greater than 10 MeV. The peak at 511 keV is due to positron annihilation and the 60 keV peak is induced by Pb fluorescence.

The absorbed dose has been evaluated in each TLD. Then a conversion factor equal to 1.14 (air kerma per dose absorbed in TLD700) from literature has been applied [6].

Figure 2.5. Photon and secondary electron energy spectra per primary electron per each TLD batch

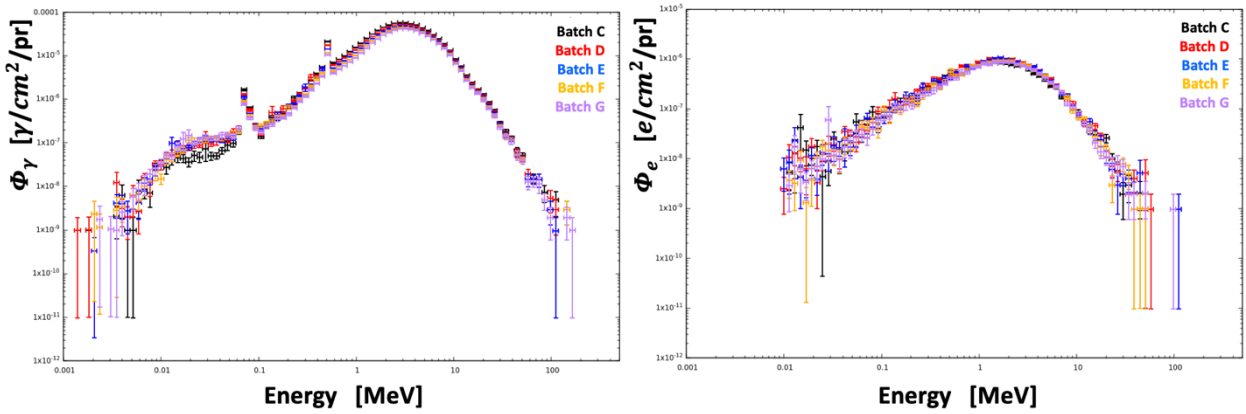

2.6. Experimental setup – 2

We repeated a similar test in BTF in June 2022, but evaluating both the gamma and neutron induced dose and both behind and to the side of the Pb target. For this test, 30 TLD700s and 30 TLD600s have been used. These have been divided in 6 plastic holders (similar to the previous test, Fig.1.2, top-left) with 5 TLD700s and TLD600s each (for a total o 10TLDs/holder). Then, during the exposure, the holders have been inserted in the middle of ~ 15 cm diameter polyethylene cylinders (height ~ 15 cm), in order to maximize TLD600 sensitivity and detection efficiency to neutrons. The calibration with the Am-Be source has been done in the same geometry.

As reported in Figure 2.6, right, two cylinders per run have been placed in the BTF, one behind the ~ 16 cm lead target (at 0°), similar to setup-1, and the other one to the side (at 90°), thanks to the BTF laser alignment system for the positioning. Three runs were performed, corresponding to three different charge intervals, up to 3.2 x 10^{12} e^-. The batches placed behind the target have been named D1, D2 and D3. The ones to the side, L1, L2 and L3.

Again, a complete FLUKA model of the setup has been performed (version 2021.2.5), as described in the previous section, but considering the new configuration and geometry (Fig. 1.6, left), including the polyethylene cylinders. The air kerma is evaluated as reported in setup 1 and neutron ambient dose equivalent has been scored in the air volumes as the one of the entire cylinders. The photons (neutrons) energy spectra evaluated with FLUKA per primary electron is reported in Figure 2.7-left (right), entering the TLD matrix (referred to the whole polyethylene cylinder).

For this test, the calibration has been performed both with a Cs-137 source for photons and with an Am-Be for neutrons. The neutron induced ambient dose is evaluated from TLD600s counts, subtracting the gamma induced counts estimated through the TLD700s.

The measurements result due to photons dose are summarized in Table 2.3, both for 0° and 90°. The kerma values in the third columns are the average over the 5 TLD700s per batch. The relating standard deviation is reported in the fourth column. The last two columns show the same quantities estimated with FLUKA.

The measurements of neutrons ambient dose equivalent are evaluated through the TLD600s glow curve integrals and subtracting the amount of counts due to photons (evaluated by the TLD700s). The results are reported in Table 2.4.

Both the results for gamma and neutrons at 0° and as a function of the integrated primary beam charge are reported in Figure 2.8 too, in the left and right panels, respectively.

Figure 2.6. FLUKA model (left) and real picture (right) of the experimental setup-2

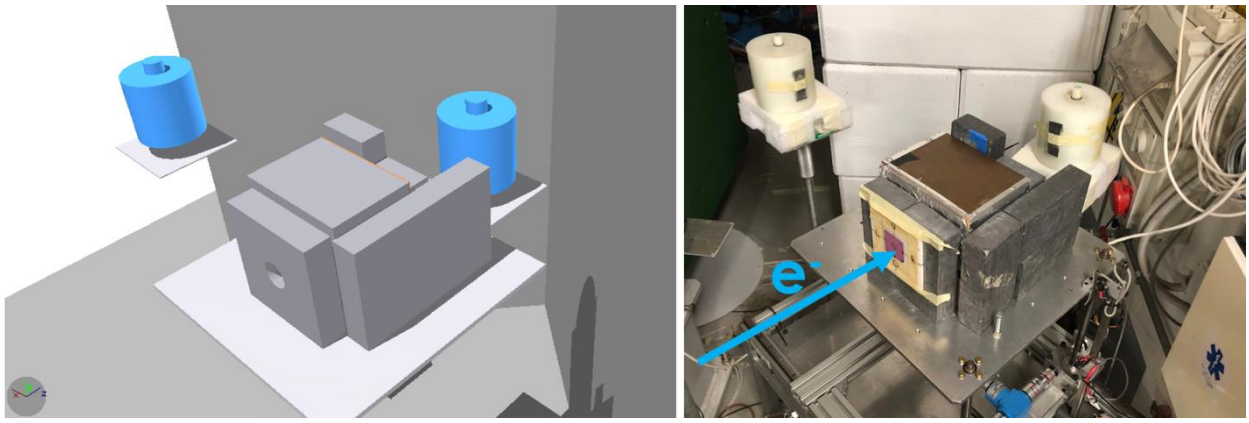

Figure 2.7. Left: Photon energy spectra per primary electron entering the TLDs matrix. Right: neutron energy spectra per primary electron referred to the entire cylinders volume.

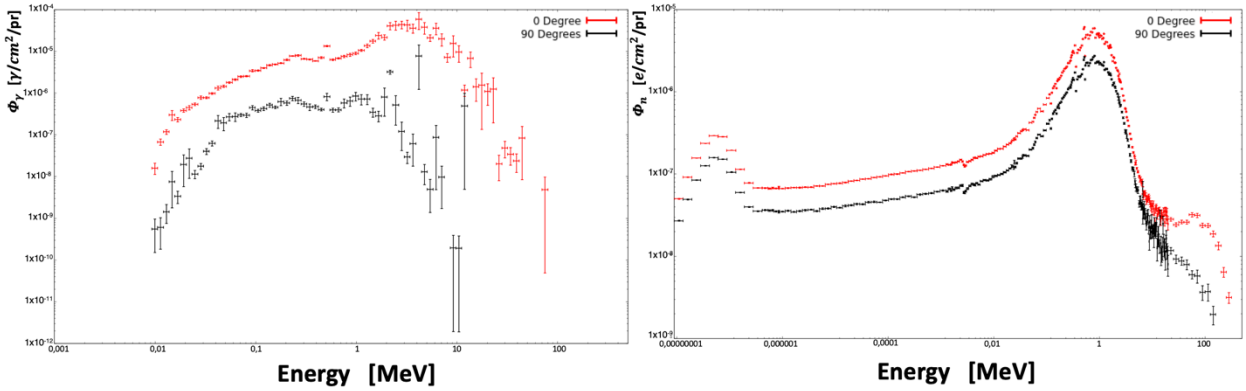

Table 2.3. Summary of the air kerma results for each batch of the first test

Batch	Charge [#e$^-$]	Kerma $_{exp}$ [mGy]	σ_{exp} [mGy]	Kerma $_{FLUKA}$ [mGy]	σ_{FLUKA} [mGy]
D-1	1.01E+12	2.64	0.40	2.92	0.03
D-2	2.04E+12	5.81	0.87	5.84	0.06
D-3	3.02E+12	10.05	1.51	8.76	0.09
L-1	1.01E+12	0.28	0.04	0.07	0.01
L-2	2.04E+12	0.41	0.06	0.14	0.01
L-3	3.02E+12	0.59	0.09	0.21	0.02

Table 2.4. Summary of the neutron induced ambient dose results for each batch of the first test

Batch	Charge [#e$^-$]	D $_{exp}$ [mGy]	σ_{exp} [mGy]	D $_{FLUKA}$ [mGy]	σ_{FLUKA} [mGy]
D-1	1.01E+12	5.05	0.76	4.31	0.40
D-2	2.04E+12	10.00	1.50	8.62	0.90
D-3	3.02E+12	13.44	2.02	12.93	1.30
L-1	1.01E+12	2.70	0.41	2.01	0.20
L-2	2.04E+12	5.47	0.82	4.02	0.04
L-3	3.02E+12	7.49	1.12	6.03	0.06

Figure 2.8. Data-MC comparison of the measured kerma as a function of the integrated primary beam charge impinging on the lead target

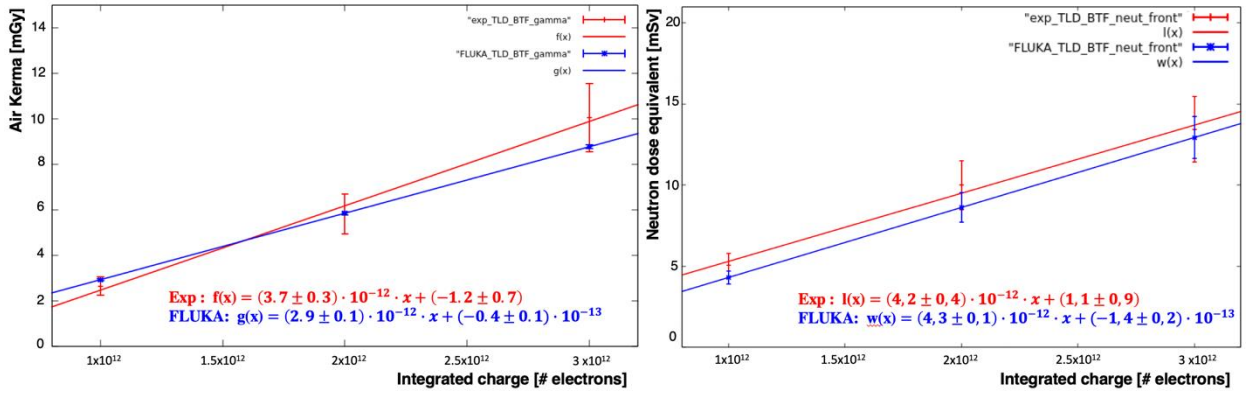

2.7. Summary and Conclusions

A good agreement between data and MC evaluation through FLUKA (version 2021.2.5) is clearly visible, both for the first test of February 2022 (setup 1) and the second one in June 2022 (setup 2) at 0°.

In the first setup, a conversion factor of 6.13×10^{-12} mGy/e- (with 16.6 cm of Pb + 2 mm Cu) has been estimated. The calibration performed with the 661 keV photons of the Cs-137 source resulted to suit also for the higher energy BTF photon spectrum, validated by the FLUKA-MC evaluation.

In the last setup, a conversion factor of 3.7×10^{-12} mGy/e- has been estimated at 0° for photons. The reduction of this factor, respect to the February-22 one, is mostly due to the polyethylene moderator. Moreover, in the June configuration, a conversion factor of 4.2×10^{-12} mSv/e- from integrated primary beam to neutron ambient dose equivalent has been evaluated.

A good data-MC agreement is also visible for the neutron ambient dose equivalent at 0°. Both photon and neutron results at 90° are still under investigation, in order to better understand the not complete data-MC agreement. This setup at 90° is more sensitive to beam-target misalignment and discrepancies between measured and real distances, especially when entered and compared to simulations. Anyway, we intend to improve simulation details and to repeat the test up to higher primary charge ranges, in order to increase the TLDs counting statistic and reduce fluctuations and uncertainties.

2.8. Acknowledgments

We thank the BTF staff of the National Laboratories of Frascati for providing the beam time and the collaboration, in particular B. Buonomo, N. Di Giovenale, C. Di Giulio and L. Foggetta, for great support during the test beam data taking.

2.9. List of references

[1] B. Buonomo et al., “The Frascati Beam Test Facility new line: from design to beam commissioning”, BIC2021, Pohang, Rep. of Korea, JACoW Publishing, ISBN: 978-3-95450-230-1, doi:10.18429/JACoW-IBIC2021-MOPP05

[2] S. W.S. McKeever et al, “Thermoluminescence:dosimetry materials”properties and uses”, Nuclear Technology Publishing, 1995, ISBN 1 870965 19 1

[3] www.fysik.dtu.dk/english/research/radphys/research/radiation-instruments/tl_osl_reader

[4] T.T. Böhlen *et al., "The FLUKA Code: Developments and Challenges for High Energy and Medical Applications",* **Nuclear Data Sheets 120, 211-214 (2014)**

[5] A. Ferrari *et al., "FLUKA: a multi-particle transport code"***, CERN-2005-10 (2005), INFN/TC_05/11, SLAC-R-773**

[6] A. Herrati et al., “Investigation of TLD-700 energy response to low energy x-ray encountered in diagnostic radiology “, Open Phys. 2016; 14:150–158, doi:10.1515/phys-2016-0016

2.10. List of abbreviations and acronyms

INFN	National Institute for Nuclear Physics
LNF	National Laboratories of Frascati of INFN (Italy)
BTF	Beam Test Facility

3. Measurements and Monte Carlo Evaluations of Shielding Concrete Radioactivation in a Nuclear Physics Facility to verify the Clearance Levels

Renata Leanza[1*], Salvatore Russo [1], Giorgio Russo [1,2]
[1]INFN, Laboratori Nazionali del Sud, Via S. Sofia 62, 95123 Catania, Italy
[2]CNR-IBFM C.da Pietrapollastra Pisciotto, 90015 Cefalù (PA), Italy
[*]rleanza@lns.infn.it

The National South Laboratory (LNS) of Italian National Institute for Nuclear Physics (INFN) is a facility devoted to research activities in different field of Physics. The main particle accelerators are a K800 Superconducting Cyclotron (CS) and an electrostatic 16 MV Van der Graaf Tandem. Some LNS concrete shields of experimental rooms have been demolished due to an upgrade of the Cyclotron. In order to dispose of concrete, measurements and estimations of residual radioactivity have been carried out to verify the clearance levels (Masumoto, 2003; IAEA, 1999; Shiomi, 2000; Carbonez, 2012; Blaha, 2014).

The radioactivity quantity, gamma-emitting, has been measured with a HPGe detector. Furthermore, to estimate the presence of pure beta-emitting radionuclides, impossible to be detected by HPGe, and to confirm the measurements made for the gamma-emitting radionuclides, Monte-Carlo FLUKA simulations have been carried out. Moreover, to determine the Minimum Detectable Activity (MDA) for the HPGe measurements and to confirm the reliability of simulation, a sample of concrete identical to the demolished one was prepared and irradiated with a high intensity field of a known Am-Be source.

The results, even in the worst condition of the CS beams, show that the concrete is in conditions of no radiological relevance and could be disposed. In this work we present the performed simulations and the measurements.

3.1. Introduction

Some LNS concrete shields of experimental rooms have been demolished for a CS upgrade for maximum current. The shields (floor and prefabricated blocks, shown in Figure 3.1) could be radioactive because they have been exposed to secondary neutron fields generated by the experiments carried out during the last 30 years of LNS activity. The activation concentration of the demolished concrete is about 10^6 Bq/g (or lower) for each possible radionuclide. In this work we describe the procedures and methods of radiological characterization related to the concrete that was used for the shielding and is planned to be disposed. The values of radionuclide concentration measured with HPGe are lower than clearance levels, and simulated values match the measured values perfectly.

3.2. Procedures and Methods

- **Identification of the concrete to be disposed**

The experimental rooms involved in the disposal of concrete are highlighted in yellow in Figure 3.1.

The fixed perimeter screens (with green hatching) will remain unchanged. The mobile screens (also green) which separate the experimental rooms, made of concrete blocks, have

been removed and subsequently reused for the new screens. The floor, highlighted in yellow in Figure 3.1 have been demolished and rebuilt.

Figure 3.1: Plan of the experimental room involved in the disposal of concrete.

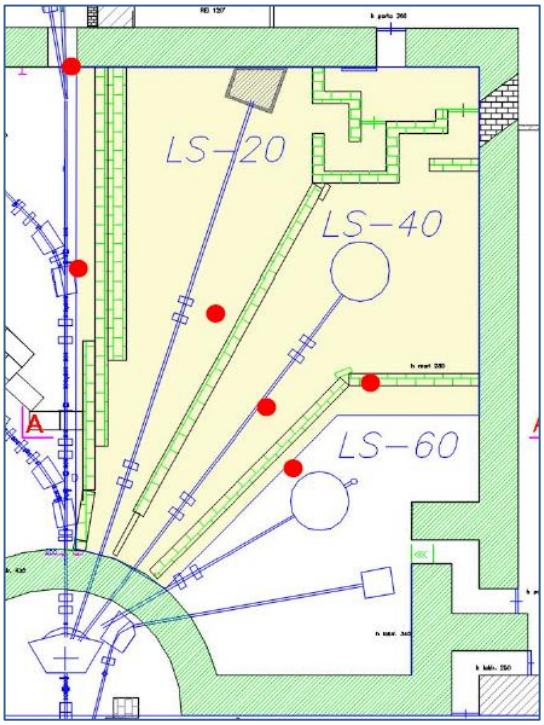

• **Determination of the workloads**

In order to correctly evaluate the neutron fields (Bedogni, 2012; Amgarou, 2011) produced during the last 30 years of operations, an identification of the workloads of the experimental rooms involved in the upgrade have been carried out.

The main accelerated beams have been obtained from the official LNS calendars:

- Until 1995 all the beams (protons to 197Au) have been accelerated by the Tandem, the only machine in operation, with energies depending on the voltage applied to the terminal which had maximum values of 14-15 MV and on the charge states of the ions, therefore the energies ranged from several MeV/amu for the heavy ions up to a maximum of 28 MeV/amu for the protons.

  - Since 1995 the cyclotron has also come into operation and the beams accelerated have been mainly from 12C to 197Au with energies of a few tens of MeV/amu and currents on the order of a few tens of nA for the light beams to a few hundreds of nA for the heavy beams with higher charge state. The beams have been stopped in 2020 during the Covid-19 pandemic. As a precaution, however, a downtime of only 6 months in the period from June to December 2020 has been considered.

  - In the 20-degree experimental room only 4 experiments have been carried out for a total of 11 days (from 2010 to 2012).

- 40-degree experimental room has been used only for 6 shifts, until May 2018, for a total of a few days. After 2018 it was no longer used.

- With concern to the diffuse neutron fields present in the experimental rooms and coming from the experiments carried out in the adjacent rooms (0° and 60°), it is underlined that these fields have been mainly due to the reflection from the roof and the walls, and the skyshine.

• **FLUKA simulations**

The Monte-Carlo code FLUKA simulations have been carried out to estimate the gamma and beta-emitting radionuclides and the residual activation.

The residual activation in the concrete would be produced only from its irradiation by ambient neutron fields. In each experimental room one or more fixed environmental detectors have been operated continuously for the entire 30-year period (in Figure 3.1 the red points indicate their position). The detectors are REM-counters, with counter proportional BF3 or He3 surrounded by polyethylene moderator. They have recorded the environmental dose equivalent H* in each room with typical integration times of 2-5 minutes. The recorded values give us the total dose due to ambient neutrons for the entire period of the accelerator operations.

Figure 3.2: Some examples of neutron H* simulated for Tandem and CS beams.

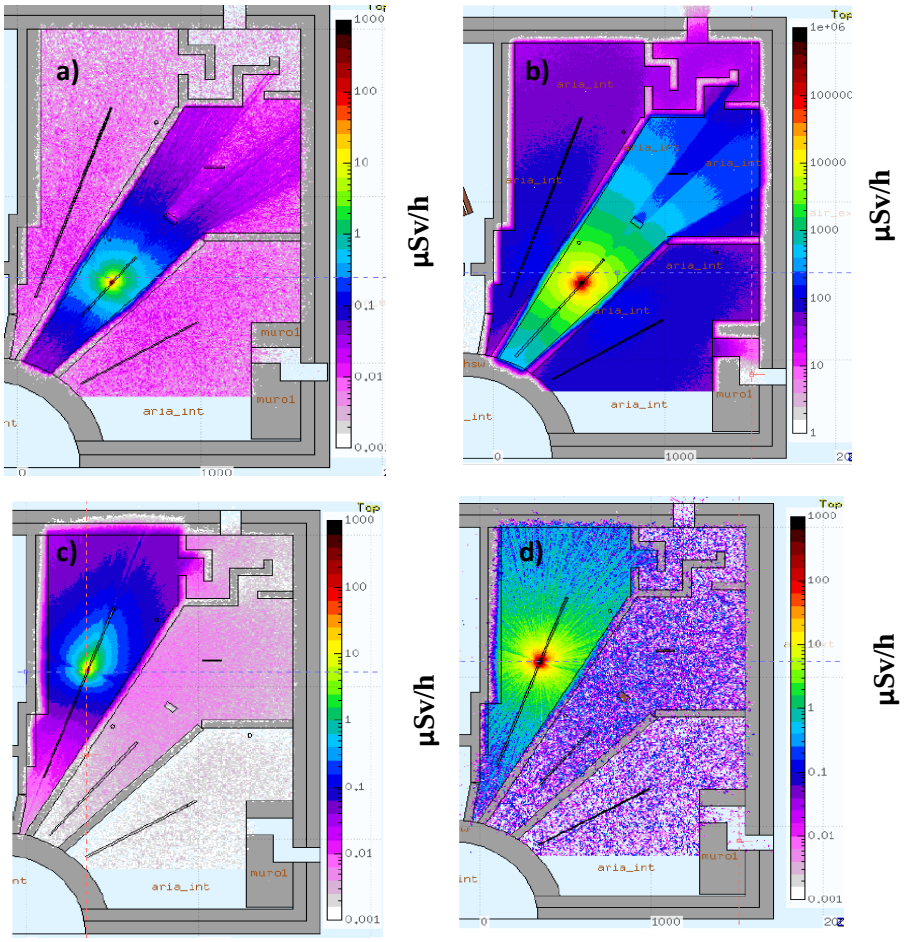

A simplification of the last 30-year experiments has been simulated. Since it was impossible to carry out a single simulation that included the different beams sent to the experimental rooms for the various experiments, several simulations have been made, reproducing the typical experiments, with irradiation profiles corresponding to the real ones and producing an accumulated dose identical to that measured in the same points where the fixed environmental detectors were positioned. At the end the values obtained have been summed.

Figure 3.2 shows an example of the neutron ambient dose equivalent, H*(10). Panel a) shows a Carbon beam in 40-degree experimental room with Tandem; panel b) shows a proton beam in the 40-degree experimental room with CS; panel c) shows a Carbon beam in the 20-degree experimental room with CS; panel d) shows a Carbon beam in the 20-degree experimental room with Tandem.

In Figure 3.3 the simulated radionuclide concentrations are shown. Maximum radionuclide concentration is about 1E-6 Bq/g, three orders of magnitude lower than clearance levels.

Figure 3.3: Simulated radionuclide concentrations

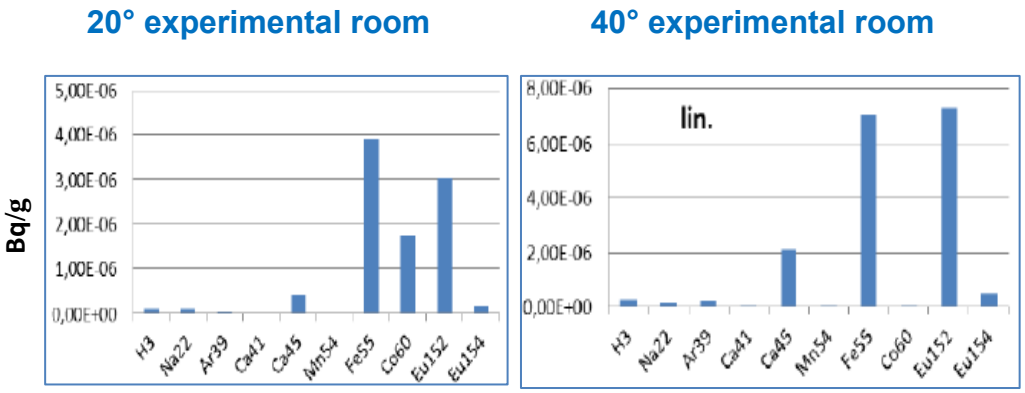

- **Sampling**

The samplings have been taken with demolition of the necessary concrete quantity of surface which was more exposed to the neutron fields. For the floor sample, one of every two cubic meters of material to be disposed have been taken, which is equivalent to a sample for every 4 m^2 of surface (one for each square identified in the grid shown in Figure 3.5 where the floor is demolished); meanwhile for the blocks a sample for each cubic metre for every two adjacent blocks have been taken (Report EUR 19151, 1999).

Figure 3.4: Demolished concrete and blocks

Figure 3.5: Grid of the LNS 20 and 40-degree experimental room (left) and Magnex experimental room (right), involved in the demolishing of the concrete shields. In order to determine the samples for the floor sample, one of every two cubic meters of concrete and for the blocks one cubic metre for every two adjacent blocks have been taken.

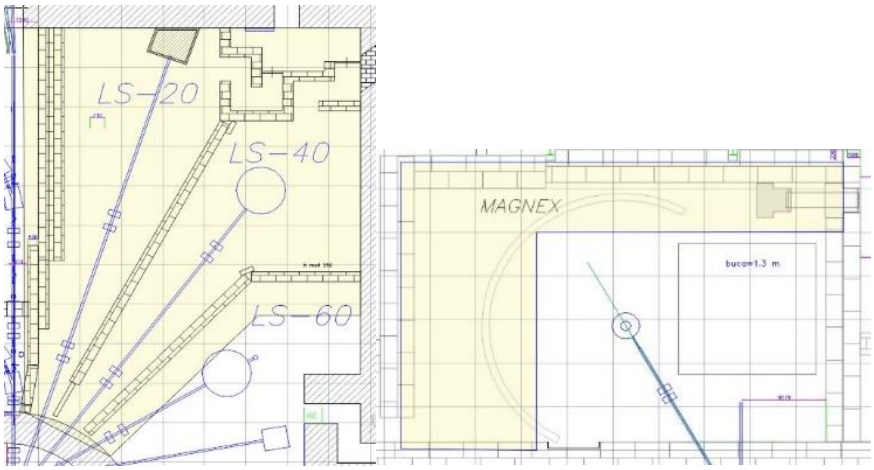

The concrete to be disposed have been crushed into small pieces and placed in 1 liter Marinelli beakers (Figure 3.6).

Figure 3.6: Concrete is crushed and placed in 1 liter Marinelli beakers.

The net weight contained in each beaker is approximately 1.5 kg (the density of crushed material is lower than the density of concrete as a whole because the crushed concrete is loosely packed inside the beaker); each beaker contains material taken from a single point.

The choice of this geometry is given by the reproducibility of the measurements and the possibility of having the calibration in the same geometry using Marinelli calibration sources and using a specific software (ANGLE) to convert the efficiency curves obtained from the sources with the specific density and chemical composition of the concrete.

- **HPGe calibration and Minimum Detectable Activity (MDA) determination**

For the measurements of the samples to dispose, a high efficiency hyperpure germanium (HPGe) detector has been used as indicated in ISO 19017 (2017), Klett (2005), as it is an excellent and sensitive technique for qualitative and quantitative analyses, including various concrete types.

The HPGe detector have been calibrated and the Minimum Detectable Activity (MDA) have been determined for each radionuclide. A sample of concrete identical to the demolished one (blank) has been prepared and irradiated with a high intensity field of a known Am-Be source (Koichi, 2016; Kinno, 2000; Pai, 2016; Go Yoshida et al., 2020). The measurements of these samples (in the same Marinelli geometry) detect the peaks of radionuclides produced by neutron activation and give us the MDA values of our system for the measuring time of 24 hours.

ORTEC gamma-vision programs have been used to analyse the spectrum acquired and to determine the MDA values (ISO 11929, 2021).

Figure 3.7 shows a comparison between the spectra of the blank sample (a) and the spectra of irradiated sample (b) where the peaks of artificial radionuclides can be clearly identified.

Figure 3.7: a) Peaks of natural radionuclides in blank concrete; b) Peaks of radionuclides produced by Am-Be activation after about one month cooling time after irradiation.

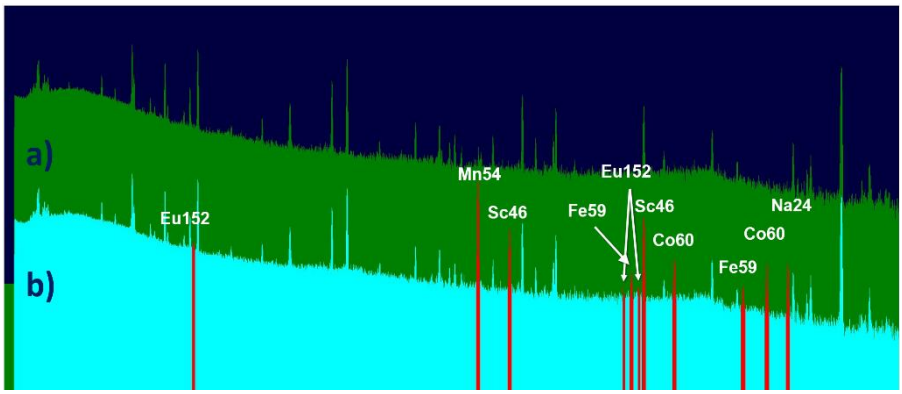

Table 3.1: Concentration activity of the irradiated sample.

	kBq/kg
Na24	0,0041
Sc46	0,0171
Mn54	0,0436
Fe59	0,0032
Co60	0,0034
Eu152	0,0033

Moreover, in order to compare the activation values produced by the irradiated sample, FLUKA Monte Carlo simulations have been carried out.

Figure 3.8, panel a) shows the geometry of the FLUKA simulation; panel b) shows a histogram of radionuclide concentration, Bq/g, as a function of the mass number, A. Panel c) shows the same concentration as a function of the mass number, A on the x axis and atomic number Z on the y axis.

The simulated values match the measured values perfectly. Moreover, FLUKA simulations have been used to estimate beta-emitting radionuclides. Radionuclides with a short half-life are present in the simulated sample, while they do not exist in the irradiated one due to the time elapsed after the irradiation.

Figure 3.8: a) Geometry of the FLUKA simulation, b) and c) activation produced by irradiating the sample after 4 days cooling time.

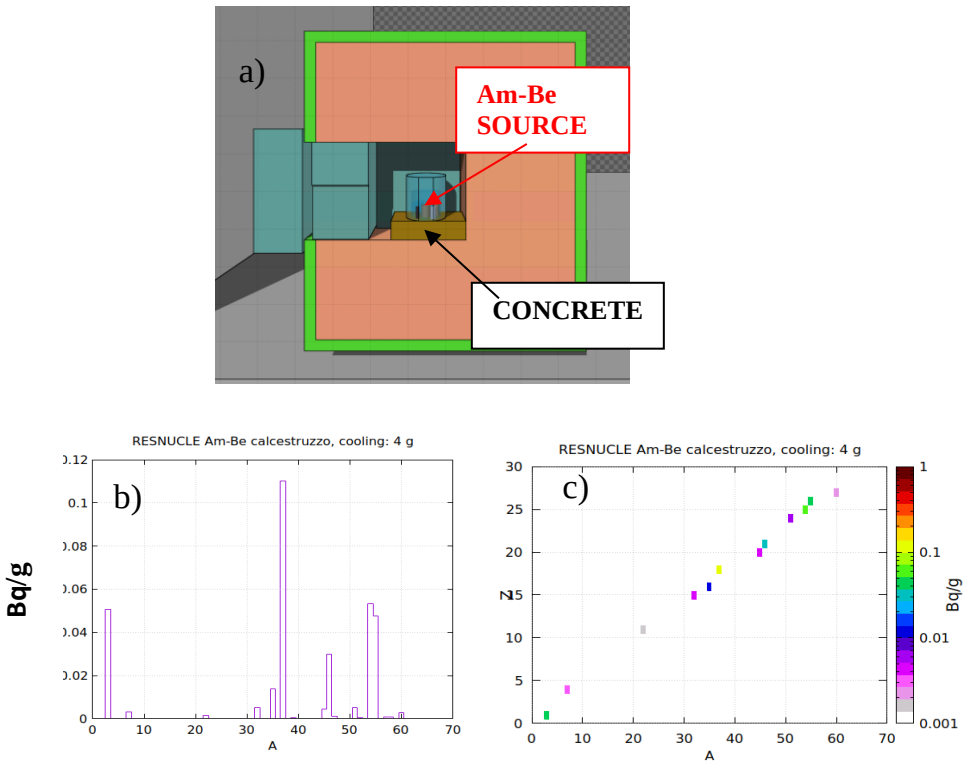

- **Measurement of activity with a gamma spectrometry system for the determination of gamma emitting radionuclides.**

As expected, all the measurements of the disposable concrete samples revealed only the presence of natural radionuclides and the artificial ones below the MDA levels.

For gamma-emitting radionuclides the MDA values that will be used in the calculations of the individual measurements of the samples to be disposed will be those provided for each specific measurement from analysis software, while for the beta emitters (shown in green in Table 3.2) the activity values have been obtained from the relationships with the reference value of Co-60 quantified by simulations (shown in Table 3.1).

In Table 3.2, the radionuclides are reported in the column 1 (Carroll, 2001), the concentration for each radionuclide is reported in column 2, the clearance levels are in column 3, and the ratios between the values of MDA and the clearance level are in column 4. The weighted sum of all radionuclides highlights that our systems are able to detect with good reliability values lower than one order of magnitude of the clearance levels according to ISO calculations and two orders of magnitude according to ORTEC calculations.

Table 3.2: MDA values from the irradiated sample and ratios between the MDA values and the clearance levels for each radionuclide.

	MDA ISO (KBq/Kg)	Clear Level (KBq/Kg)	MDA/CLLev ISO
H3	0,00015	1,0	0,00015
Na22	0,00040	0,1	0,00400
Ar39	0,00011	0,1	0,00114
Ca41	0,00001	1,0	0,00001
Ca45	0,00103	1,0	0,00103
Mn54	0,00062	0,1	0,00620
Fe55	0,00451	1,0	0,00451
Co60	0,00075	0,1	0,00748
Eu152	0,00361	0,1	0,03610
Eu154	0,00188	0,1	0,01880
		Sum	0.079

3.3. Conclusions

This work demonstrated that in our research laboratory, while operating heavy beam accelerators for more than 30 years, the concrete shields and floors of the experimental rooms are not radioactive and can be disposed.

The Monte Carlo simulations have been used to reproduce the typical LNS experiments of the last 30 years, obtaining an accumulated dose comparable with the measured one in the same locations where the fixed environmental detectors were positioned. Essentially, the

Monte Carlo simulations have been used to determine the radionuclide concentrations in the floor and in the shielding blocks that have to be disposed.

The Monte Carlo radionuclide concentrations have been validated comparing values with the HPGe detector measured ones. The agreement between the calculated and measured data validated the code and proves its reliability in the case of complex systems.

3.4. List of references

K. Masumoto et al. (2003), "Evaluation of radioactivity induced in the accelerator building and its application to decontamination work" J. Radioanal. Nucl. Chem. Vol. 255, No. 3, p. 465–469

IAEA SAFETY STANDARDS SERIES No. WS-G-2.2 (1999) "Decommissioning of medical, industrial and research facilities."

T. Shiomi et al (2000), "Measurement of Residual Radioactivity of Machine Elements and Concrete on the Cyclotron Decommissioning" Journal of Nuclear Science and Technology", Supplement 1, p. 357-361

P. Carbonez et al, (2012) "Residual radioactivity at the CERN 600MeV synchro-cyclotron" Nuclear Instruments and Methods in Physics Research A 694, p. 234–245

J. Blaha et al (2014), "Long-term residual radioactivity in an intermediate-energy proton linac", Nuclear Instruments and Methods in Physics Research A 753, p. 61–71

R. Bedogni et al. (2012), "Measurement of neutron spectra generated by a 62 AMeV carbon – ion beam on a PMMA phantom using extended range Bonner sphere spectrometers". Nuclear Inst. and Methods in Physics Research, A, Volume 681, p. 110-115.

K. Amgarou et al. (2011), "Measurement of the neutron fields produced by a 62 MeV proton beam on a PMMA phantom using extended range Bonner sphere spectrometers". Nuclear Inst. and Methods in Physics Research, A, Volume 654, p. 399-405.

Report EUR 19151 (1999), European commission: Nuclear Safety and the environment, "Evaluation of the Radiological and Economical Consequences of Decommissioning Particle Accelerator" VUB –Brussels.

ISO 19017 (2017), "Guidance for gamma spectrometry measurement of radioactive waste".

A. Klett et al. (2005), "A New Contamination Monitor With Scintillation Detection" IEEE Nuclear Science Symposium, San Juan, Puerto Rico, October 23- 29, 2005.

O. Koichi et al. (2016), "Activation experiment for concrete blocks using thermal neutrons" ICRS-13 & RPSD-2016, 13th International Conference on Radiation Shielding.

ISO 11929 (2021), "Determination of the characteristic limits (decision threshold, detection limit and limits of the coverage interval) for measurements of ionizing radiation".

T. Shiomi et al. (2000), "Measurement of Residual Radioactivity of Machine Elements and Concrete on the Cyclotron Decommissioning", Journal of Nuclear Science and Technology, Supplement 1, p. 357-361.

Q. Wang et al. (2007), "Evaluation of the radioactivity in concrete from accelerator facilities". J. Radioanal. Nucl. Chem., 273, p. 55-58.

Kinno and al. (2000), "Studies on induced activities and target nuclei in low-activation concrete structure for thermal neutron irradiation" J. Nucl. Sci. Technol. 30(1), p. 821-826.

Go Yoshida et al. (2020), “Investigation of variations in cobalt and europium concentrations in concrete to prepare for accelerator decommissioning”, Journal of Radioanalytical and Nuclear Chemistry 325, p. 801–806.

L. R. Carroll (2001), “Predicting Long-Lived, Neutron-Induced Activation of Concrete in a Cyclotron Vault”, Sixteenth international conference on the application of accelerators in research and industry. AIP Conference Proceedings, Volume 576, pp. 301-304.

Pai B H V et al. (2016), “Estimation of trace element concentration and neutron induced radioactivity in rock samples of different geological compositions for neutron shielding”, Indian Journal of Pure & Applied Physics Vol. 54, January 2016, pp. 7-14

3.5. List of abbreviations and acronyms

INFN	National Institute of Nuclear Physics
LNS	Laboratori Nazionali del Sud
CNR-IBFM	Consiglio Nazionale delle Ricerche -Institute of molecular bioimaging and physiology (IBFM)
MDA	Minimum Detectable Activity
HPGe	Hyperpure germanium

4. Methodology and preliminary studies for the evaluation of induced radioactivity for the decommissioning of Synchrotron SOLEIL storage ring

Jean-Baptiste Pruvost[1*],
[1]Synchrotron SOLEIL
[*]jean-baptiste.pruvost@synchrotron-soleil.fr - corresponding author

The upgrade of Synchrotron SOLEIL [1] towards a Multi-Bend Achromat lattice and very low emittance (~80 pm.rad) electron beam synchrotron light source will led to the decommissioning of the present storage ring. In France, it is mandatory before the shutdown to submit to the French Nuclear regulation Authority (so call ASN) an authorisation application for both the decommissioning of present storage ring and to operate the new one. In French regulation, there are no clearance levels for induced radioactive solid materials, but for few months, there is a brand-new regulation[2] that allows nuclear waste recovery only for very low induced radioactivity of metallic materials if able to be recycled by a dedicated industrial partner. In order to get both the deconstruction authorisation and to recover valuable metallic materials from the tunnel, a detailed study is conducted, relying on Monte Carlo simulations thanks to the capabilities of FLUKA4-2[3,4] code with as realistic as possible physical conditions observed during operation. This study is completed with measurements on present machine for beam losses distributions and residual activity measurements on equipments already removed from the ring with a well-known irradiation history that will be reproduced in FLUKA and compared to calculation results. All this should bring the demonstration of reliability of our methodology to get ASN final agreement to proceed.

4.1. Introduction

Synchrotron SOLEIL is the French 3rd generation synchrotron light source operating in a 354 m circumference storage ring a 2.75 GeV electron beam and 29 beamlines since 2009 for French and worldwide scientific users. The upgrade of Synchrotron SOLEIL storage ring will enhance its performances up to a 4th generation diffraction limit storage ring (DLSR) with very low emittance electron beam, very high brilliance, and coherent synchrotron light source. Prior to the building of this new ring, the present storage ring must be decommissioned. The methodology and preliminary results presented in this paper are dedicated to the radiation safety studies that are mandatory for being cleared by the French nuclear authority before starting the decommissioning.

4.2. Material and Methods

This radiation safety study will be performed with a very extensive use of the FLUKA Monte Carlo code for the induced activity produced by the electron beam losses and for the residual dose rates generated by the induced radioactive nuclides.

This study will be enriched by measurements of beam loss distribution along the storage ring, residual activity measurements by gamma spectroscopy and, when possible, by liquid scintillation for beta emitters.

3D Modeling

A very detailed geometry of the storage ring is under construction in FLUKA using FLAIR[5] as shown for a typical cell of the storage ring in Figures 4.1, 4.2 and 4.3 below. Vacuum pipes, bending magnets (BM), quadrupole magnets (QP), sextupole magnets (SP), insertion devices like undulators (electromagnetic or permanent magnets) or wigglers, girders and so on are modeled in detail to fulfill ASN requirements.

Figure 4.1. Detailed 3D model of a storage ring cell and concrete tunnel

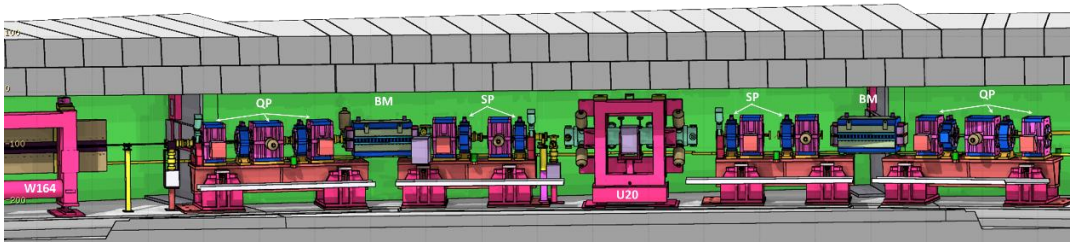

Note: The figure above is showing FLUKA model of cell C06 of the storage ring, not yet achieved. One can see from left to right, the end of SDM6 straight section with the jaws of W164 wiggler, the upstream half arc, the SDC6 short straight section with an in vacuum U20 undulator, and the downstream half arc leading to the straight section (SDM7) of cell C07. (3D view obtained with FLAIR)

Figure 4.2. Detailed 3D model of a bending magnet

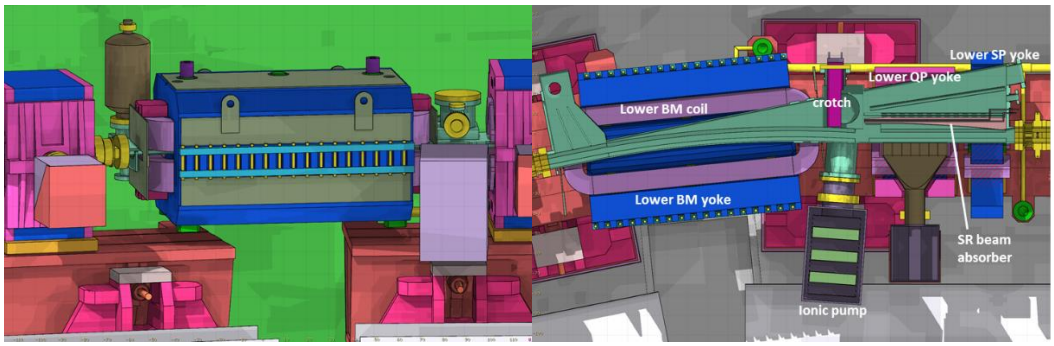

Note: On left-hand side picture, one can see a close-up of the 3D model of a BM and, on the right-hand side picture, a horizontal cut of its complex vacuum chamber with the crotch and the synchrotron radiation (SR) beam absorber.

Additionally, more than 90 user customized materials have been described so far in FLUKA to consider the actual materials and particularly the different aluminum, copper, steel and stainless-steel grades used for the components of the storage ring.

Two examples of specific grades described in FLUKA input format are shown below. M1200 corresponds to the soft iron grade used to build the magnet yokes and SS316LNb refers to the stainless steel (SS316LN grade as referred in AISI)

```
MATERIAL                              7.80        67                    M1200
COMPOUND     -0.98325       IRON     -0.013   SILICON     -0.002  MANGANESM1200
COMPOUND      -0.0012   ALUMINUM     -0.0005  PHOSPHO     -5E-05   CARBONM1200

MATERIAL                              7.8         81                   SS316LNb
COMPOUND     -0.63191       IRON     -0.185   CHROMIUM    -0.125   NICKELSS316LNb
COMPOUND       -0.025   MOLYBDEN     -0.02    MANGANES    -0.01    SILICONSS316LNb
COMPOUND      -0.0022   NITROGEN  -0.00045    PHOSPHO  -0.00029   CARBONSS316LNb
COMPOUND     -0.00015     SULFUR                                        SS316LNb
```

Figure 4.3. Vertical cuts of a BM and a QP

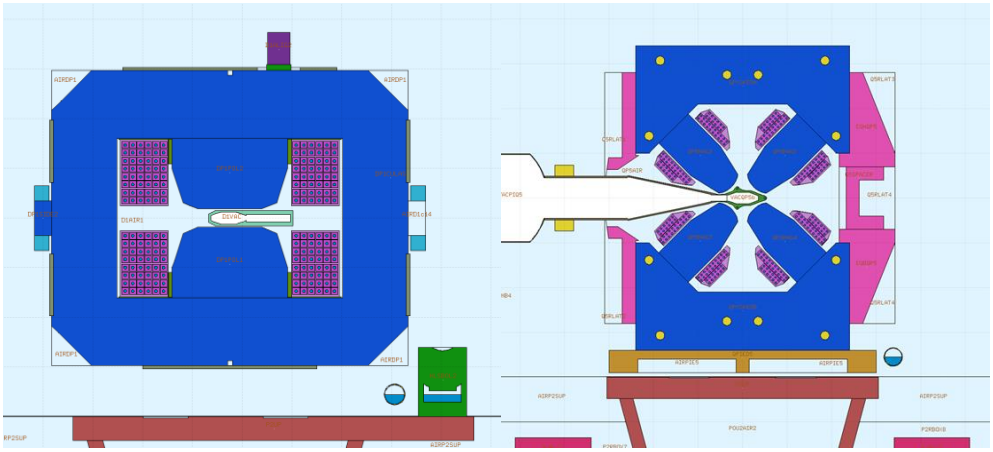

Note: Vertical cross-sections showing yoke and coil details of a bending magnet (left) and a quadrupole magnet (right) and corresponding beam pipe profiles (SS316LN and AL6060 grades resp.). All the magnet yokes are made of soft iron steel M1200 grade (>98%wt Fe). Each color here is specific to a material defined in FLUKA.

Beam losses source term definition

Electron source particles will be defined by a dedicated routine (source.f) to sample the 2.75 GeV beam losses spread along the storage ring with the relative distribution of each filling pattern as measured by beam loss monitor (BLM) network and coupled with machine physics simulation results of the phase space of lost beam particles in terms of transverse position and momentum.

Particle transport

Transport of both primaries and secondaries will take into account the effect of magnetic fields from BM, QP and SP. To achieve this, the capabilities of FLUKA to reproduced magnetic fields will be used intensively to simulate the effect of such magnetic fields on the trajectory of the charged particles generated by the beam losses into the region of interest.

4.3. Experimental results

Beam Loss Monitors

Since 2021, SOLEIL storage ring is equipped with a Beam Loss Monitor (BLM) network[6] of 80 plastic scintillator detectors spread along the ring. These BLM are made of a scintillator and a photomultiplier embedded in a compact aluminum housing and linked to a Libera electronic module installed outside of the ring to perform acquisition.

Figure 4.4. Vertical cuts of a BM and a QP

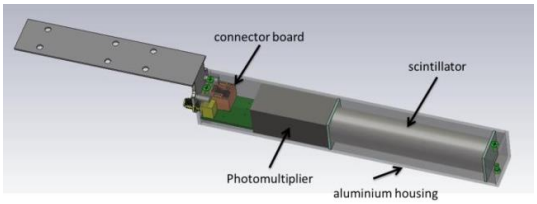

Note: Cut-off view of a BLM. All BLM are calibrated with a ^{137}Cs calibration source.

The BLM are distributed along the storage ring at the beam level in the arcs and at specific points of interest like in the injection region. This allows to display the beam losses distribution for operation analysis with respect to the storage ring configurations.

Figure 4.5. Beam Loss monitors installed inside storage ring tunnel

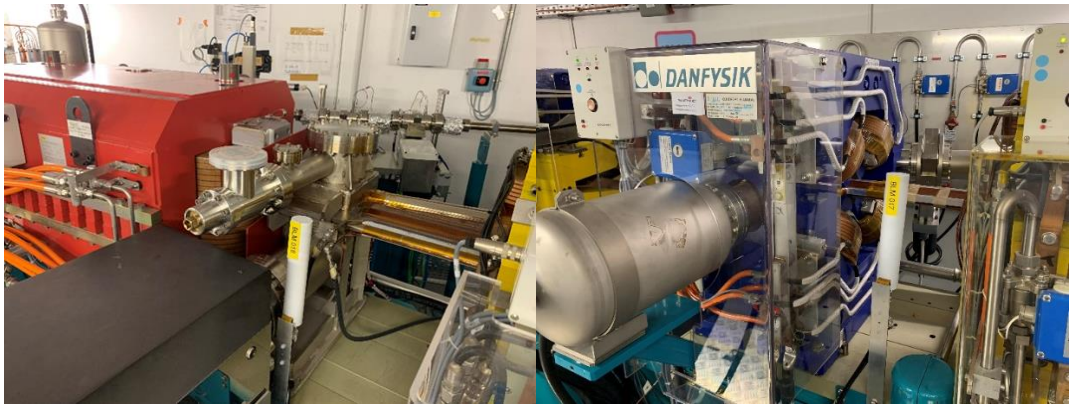

Note: On the left-hand side picture, a BLM (white cylinder) installed just downstream a bending magnet (red yoke) close to the beam pipe. On the right-hand side, a BLM installed close to a quadrupole chamber between a quadrupole magnet (blue yoke) and a sextupole magnet (yellow yoke).

Synchrotron SOLEIL operation

Synchrotron SOLEIL is providing to its users four types of storage ring filling patterns along the year, each with different beam parameters. For radiation safety point of view, beam current intensity and beam lifetime are some of the main parameters to consider, particularly in terms of continuous beam losses. The Table 4.1 below presents these parameters for the four filling patterns operated each year at SOLEIL.

Table 4.1. Main beam parameters considered for each storage ring filling patterns

Beam modes delivered	Current (mA)	Lifetime (hours)	Average total Loss rate (e-/s)	Operation
Uniform – 416 bunches	500	10.4	$6.61\ 10^{7}$	21 weeks per year
Hybrid – 312 bunches + 1 isolated	445 + 5	8.6	$7.14\ 10^{7}$	10 weeks per year
8 bunches	100	3.8	$3.41\ 10^{7}$	1 or 2 weeks per year
1 single bunch	16	2.7	$7.42\ 10^{6}$	1 or 2 weeks per year

Beam Losses distribution measurements

The beam losses have been measured during specific shifts for BLM tests and optimization and are measured and recorded daily during standard operation. User beams are delivered for 6 days continuous period and the filling pattern is able to change from one week to the next one. Measurements of the beam losses distribution are presented below for the four filling patterns delivered to users as a weekly average for each BLM.

The ordinate axis percentage refers to the proportion of the total beam losses, observed by the BLM network, detected by each individual BLM. As expected and displayed above, beam losses are concentrated in the injection region area (from BLM#1 to #10) immediately downstream of the vertical and horizontal scrapers (BLM#2 & #10 resp.). One

can see that the distributions are globally very similar from one filling pattern to another. Single bunch mode showing a slightly higher losses on vertical scraper (BLM#2) specific of the huge current set in a single bunch with the highest vertical emittance for standard operation.

Figure 4.6. Beam Losses distributions

Note: Blue histogram presents the beam losses distribution for the uniform filling pattern with a 500 mA stored beam. Green histogram presents the beam losses distribution for the hybrid filling pattern with a 450 mA stored beam. Yellow histogram corresponds to the beam losses measurements for the 8 bunches filling with a 100 mA stored beam. And red histogram presents the beam losses distribution for the single bunch filling pattern with a 16 mA stored beam.

Residual activity measurements

Gamma spectroscopy measurements will be conducted on elements inside tunnels during shutdown and outside tunnels on vacuum chambers, beam position monitors (BPM), and magnet yokes that have been retired from tunnels. These measurements will be performed with a CZT spectrometer that can be set very close to the beam pipes and/or magnet poles thanks to its small size for in situ measurements and with a Ge(Hp) spectrometer on equipment removed outside tunnels.

Some measurements will also be performed on damaged equipment by destructive methods to estimate activities of difficult to measure (DTM) gamma emitters (like ^{55}Fe) and beta emitters (^{63}Ni or ^{3}H) isotopes.

Results will be compared to Monte Carlo simulation results obtained with the complete beam history for the time the equipment spent inside tunnels.

4.4. Calculation test and preliminary results

A calculation test has been performed with FLUKA4-1.1 on a relatively small “simplified model” of a double bend achromat (DBA) arc of cell C02 just downstream of the injection region. For example, magnet yokes are “made” of pure natural iron and coils are plain, parallelepipedal and made of pure natural copper. Vacuum chamber stainless steel used was the one available from standard FLAIR material database.

Figure 4.7. 3D view of cell C02 as modelled in FLUKA

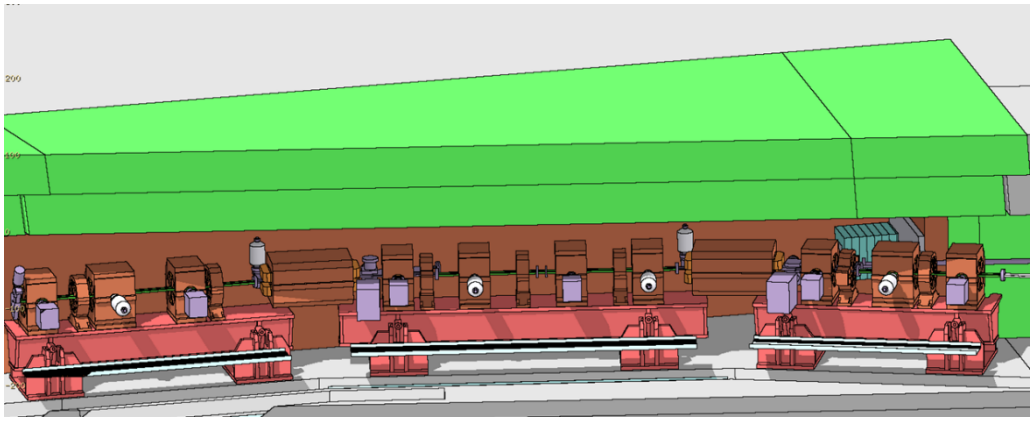

Note: FLAIR 3D view of the DBA arc of cell C02, as modelled in FLUKA, showing the complete arc with BM, QP and SP magnets, vacuum ionic pumps and supporting girders.

This first test was released with a beam losses pattern described in a source routine and roughly uniformly distributed on each segment of the arc. Electron beam particles are hitting only at beam level the inner wall of the beam pipe with an arbitrary grazing angle. Only the 1.71T magnetic field of the BM was set with MGNFIELD cards. Thus, irradiation profiles and normalisation were set for a unique complete year of operation (2020) corresponding to 5 runs and 5 shutdown periods and with 3.7% of the total beam losses concentrated in the arc for a beam lifetime of 4 hours with 500 mA stored into the ring. (Corresponding to 9.5 10^6 e^-/s)

Figure 4.8. Ambient dose equivalent rates H*(10) at beam shutdown

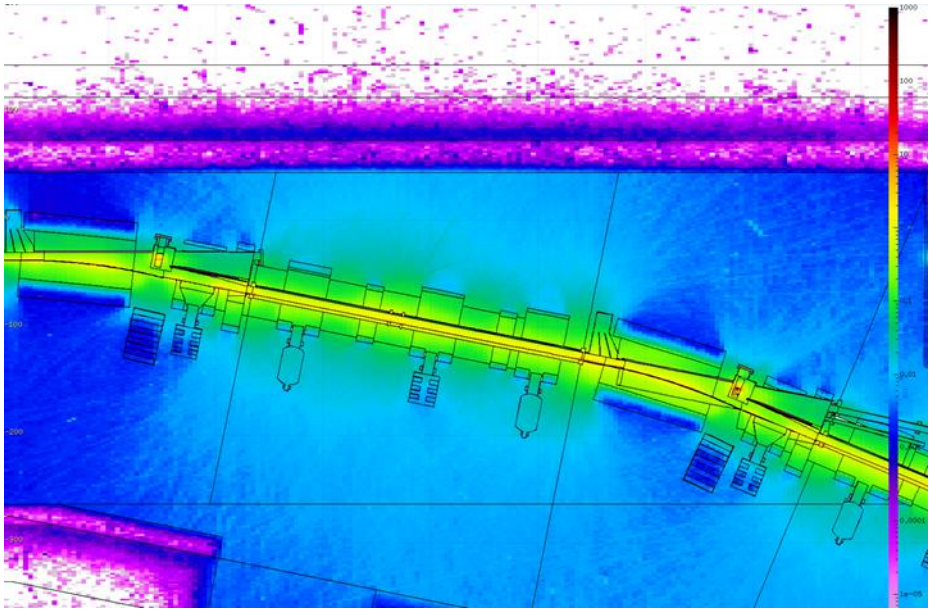

Note: Ambient dose rate color scale is displayed in µSv/h after a decay of t=0 s.

Residual radiation dose rates from induced activity were estimated with FLUKA. Above is presented, on Figure 4.8, residual ambient dose rates (from ICRP74 conversion coefficients) at beam height just after the beam shutdown (e.g., Decay time = 0 second). One can see that highest dose rates are about few micro-Sieverts per hour or less at contact of beam pipe surface. Maximum values are concentrated in the inner face of the vacuum chamber where electron primaries are hitting the wall of the vacuum chamber. Despite the rough and conservative assumptions for this preliminary calculation test, the results are slightly higher but nevertheless close to those observed by radiation surveys performed at the beginning of each shutdown prior to authorise personal access. It must be said that radiation surveys are generally performed typically one hour after the shutdown when most of the short life nuclides have decayed.

What can be seen is that the residual activity is mainly concentrated at electron impact position and in a very close vicinity around this zone. It is typically illustrated on Figure 4.9 below where residual activity is displayed at a cross section of a bending magnet chamber, BM yoke and coils.

After one month decay, the remaining activity is present in the inner wall of vacuum chamber, the edge of the poles of the BM and in the closest part of the BM yoke at beam plan level.

Figure 4.9. Residual specific activity (Bq/g) at beam shutdown

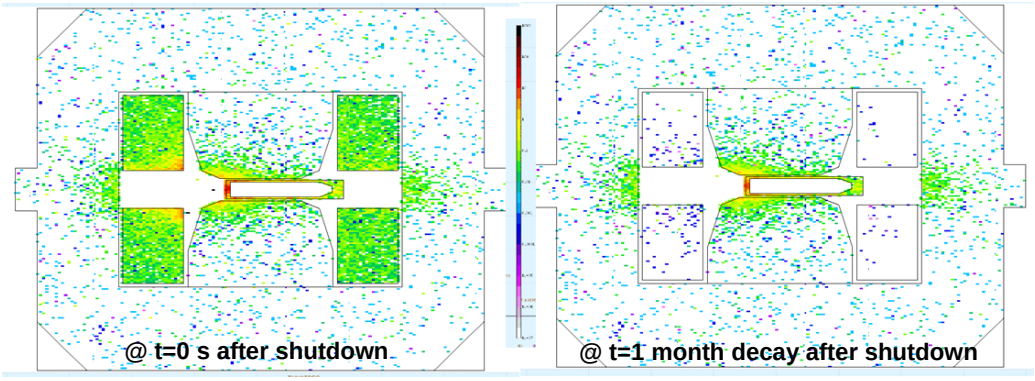

Note: Residual specific activity (Bq/g) calculated in the BM chamber, the BM yoke and coils. Consider that, for this first calculation, if the chamber is made of SS316LN grade, BM yoke is defined as pure iron and the coils are simple blocs of pure copper. One can see that very short life isotopes produced in copper have almost disappeared after 1 month decay.

Activity is mainly dominated by ^{55}Fe, ^{54}Mn, ^{57}Co and ^{51}Cr in stainless steel. Table 4.2 below is showing examples of residual activity present in this equipment for the main dominant isotopes. These examples of preliminary results were obtained for a single pole of a BM (where activity is concentrated as shown on picture above), for the complete yoke of a BM, for a stainless-steel BM vacuum chamber and for a copper alloy synchrotron radiation absorber inserted in it. (See Figure 4.2)

Table 4.2. Examples of residual activity estimated with FLUKA

Equipment (material) @decay time	Isotopes	Total activity (Bq)	Mass activity (Bq/g)	French regulation threshold (kBq/kg)
1 pole of a BM (natural iron) @t=0 s	^{55}Fe	8, 960	$3.6\ 10^{-2}$	1000
	^{54}Mn	1, 700	$6.8\ 10^{-3}$	0.1
Whole yoke of a BM (natural iron) @t=0 s	^{55}Fe	$2.06\ 10^{5}$	$7.57\ 10^{-2}$	1000
	^{54}Mn	39, 310	$1.44\ 10^{-2}$	0.1
BM copper absorber (glidcop®) @t=0 s	^{64}Cu	2, 267	1.04	100
	^{58}Co	79.9	0.037	1
BM vacuum chamber (stainless steel SS316LN grade) @t=1 month	^{57}Co	11, 910	**0.912**	1
	^{55}Fe	24, 050	1.842	1000
	^{54}Mn	6, 741	**0.516**	0.1
	^{51}Cr	24, 010	1.838	100

These preliminary results are encouraging regarding the quite low induced activity levels obtained by comparison to the brand-new French regulation thresholds (as clearance levels from EURATOM Directive 2013-59 but limited to metallic materials), except for the vacuum chamber where ^{54}Mn activity is slightly higher than the threshold and ^{57}Co is very close (bold values in Table 4.2 above). For the other isotopes, mass activities are typically several orders of magnitude below the corresponding thresholds.

It must be said that, though the assumption of beam losses homogeneously concentrated in one arc for a spoiled beam lifetime that can be considered as conservative assumptions, with calculations taking into account the whole operation history of SOLEIL for the last 17 years or a bit more, some isotopes may appear slightly more abundant and at least closer to the threshold.

4.5. Summary and Conclusions

This paper presents the methodology adopted to evaluate the induced activity that will be present on Synchrotron SOLEIL storage ring elements at the beginning of the shutdown for starting the upgrade of SOLEIL towards a 4th generation synchrotron light source.

A very detailed and as accurate as possible modelling of the storage ring for both 3D geometry and electron beam losses distribution based on measurements in operation is in progress. This approach is motivated mainly by the French regulation authority huge requirements in terms of residual activity controls and nuclear waste management. The storage ring 3D modelling and measurements results were presented as well as first results of preliminary simplified model and rough calculations performed with the Monte Carlo FLUKA code. These first results are encouraging but a lot of work is still to be done.

Finalize and run with FLUKA code the storage ring models.

Prepare and analyse samples for induced activity isotopes and compare the results to the one obtained with FLUKA calculations to strengthen the authorisation application for the decommissioning of Synchrotron SOLEIL storage ring.

4.6. List of references

1. Conceptual Design Report, Synchrotron SOLEIL Upgrade (2021).
2. Décret n°2022-174 du 14 février 2022 relatif à la mise en œuvre d'opération de valorisation de substances faiblement radioactives, JORF n°38, Feb. 2022.
3. G. Battistoni, T. Boehlen, F. Cerutti, P.W. Chin, A. Fassò, A. Ferrari et al. (2015), Overview of the FLUKA code, Annals of Nuclear Energy 82, 10-18.
4. C. Ahdida, D. Bozzato, F. Cerutti et al. (2022), New capabilities of the FLUKA Multi-purpose code, Frontiers of Physics 9, 788253.
5. V. Vlachoudis (2009), FLAIR: A powerful but user-friendly graphical interface for FLUKA, Proc. Int. Conf. on Mathematics, Computational Methods & Reactor Physics (M&C 2009).
6. N. Hubert et al. (2018), Test of new Beam Loss Monitors for SOLEIL, Proceedings of IBIC 2018.
7. J-B. Pruvost (2021), Radiation safety challenges involved by the upgrade of Synchrotron SOLEIL storage ring, Accelerator workshop of the French Physical Society (SFP), Roscoff, France.

4.7. List of abbreviations and acronyms

AISI	American Iron and Steel Institute (United States)
ASN	Autorité de Sûreté Nucléaire (France): French Nuclear Regulation Authority.
BM	Bending magnet
BLM	Beam loss monitors
BPM	Beam position monitors
DBA	Double Bend Achromat
DLSR	Diffraction Limit Storage Ring
DTM	Difficult To Measure isotopes
EURATOM	Treaty establishing the European Atomic Energy Community of European Union
ICRP	International Commission for Radiation Protection (ICRP74 refers to publication n°74 of the ICRP for Conversion Coefficients for use in Radiological Protection against External Radiation
MBA	Multi Bend Achromat
MGNFIELD	Magnetic field definition card name of FLUKA code used to described magnetic field.
QP	Quadrupole magnet
SFP	Société Française de Physique (France), French Physical Society
SP	Sextupole magnet
U20	In vacuum undulator insertion device with a 20 mm magnetic period
W164	Wiggler insertion device with a 164 mm magnetic period